THESIS

MACHINE-LEARNED GAS OPTICS WITH A FOCUS ON GEOSTATIONARY EXTENDED OBSERVATIONS (GeoXO) FOR IMPROVING WATER VAPOR OBSERVATIONS IN THE LOWER ATMOSPHERE

Submitted by

Dhyey Solanki

Department of Atmospheric Science

In partial fulfillment of the requirements

For the Degree of Master of Science

Colorado State University

Fort Collins, Colorado

Spring 2023

Master's Committee:

Advisor: Christine Chiu

Christian D. Kummerow
Shantanu Jathar

ABSTRACT

MACHINE-LEARNED GAS OPTICS WITH A FOCUS ON GEOSTATIONARY EXTENDED OBSERVATIONS (GeoXO) FOR IMPROVING WATER VAPOR OBSERVATIONS IN THE LOWER ATMOSPHERE

In the grand scheme of the earth-atmosphere system, there are few constituents more vital and mysterious than water vapor. Vital because of its interwoven thermodynamic, radiative, and dynamic influence on the weather and climate of the planet, and mysterious because of our limited capacity in observing its time evolution in horizontal and vertical space. The advancements in the spectral and radiometric accuracy of next-generation infrared sounders are expected to bring unprecedented value to our observational capability with improved profiling of lower tropospheric water vapor where it is most abundant.

Essential to performing satellite observations and their assimilation to dynamical models is the accurate and efficient radiative transfer calculations. In this process, calculating the atmospheric absorption by various gases is one of the most important steps. The 'line-by-line' approach of computing the influence of every absorption and emission line is operationally impractical for many observations that can contain hundreds of absorption lines. The existing radiative transfer models, therefore, use parameterized gaseous absorption using methods like pre-computed lookup tables or regression methods. The conventional methods compute channel values and can only be used for a specific sensor and channel.

Here, we present a new method of performing gas absorption calculations using machine learning that can be applied to the spectral interval of any channel. With an example spectral interval of the new water vapor channel on the upcoming GeoXO infrared sounder, we train neural networks to emulate the line-by-line layer optical depths on a consistent grid of 100 atmospheric layers defined by 101 pressure levels spanning from 1100 hPa to 0.005 hPa. We sample a diverse set of 8640 profiles around the globe for the year 2014 from the Medium-Range Weather Forecasts (ECMWF) atmospheric reanalyses dataset (ERA5) and use 80% of these profiles as training data and 20% of the profiles as validation data. We test the performance of the emulators using a completely independent set of 83 profiles from ECMWF for the year 2006-2007, known as ECMWF83 profiles that have been widely used for training the atmospheric transmittance due to gas absorptions. The atmospheric optical depth used as the truth in all datasets is calculated from the line-by-line Monochromatic Radiative Transfer Model (MonoRTM).

The evaluation results from the testing dataset show that the trained neural networks are able to predict line-by-line layer optical depths with a mean percent error of 0.47%. Radiative transfer models used for simulating satellite radiances, like Community Radiative Transfer Model (CRTM), require channel layer-to-space transmittance profiles for solving the radiative transfer equation. Transmittance profiles were calculated using the predicted line-by-line layer optical depths with a mean percent error of 0.02%. Further, the predicted values are also able to accurately calculate the channel weighting functions with the mean percent error of 0.13%. The results show the feasibility of utilizing neural networks in predicting line-by-line optical depths that can be applied for any spectral interval and can be highly useful for the designing of future sensors.

ACKNOWLEDGEMENTS

I have been very fortunate of having the support, help, and mentorship of a lot of people who deeply cared about me and my growth as a person. The person I am most thankful to is my mother, Jaimini. I am also deeply grateful to my grandparents and all my uncles, aunts, and cousins, without whom I would not reach where I am. I would like to specifically acknowledge my uncle and aunt Ravi and Rushika for deeply taking interest in my growth as a child and for all the conversations I had with them that helped me develop a curious outlook on the world and life.

I would like to acknowledge all the amazing and kind teachers that I was very blessed to have throughout my years in school and college. It is because of their passion for knowledge and their ability to inspire the joy of learning that motivated me to choose graduate studies. I would specifically like to express my deep gratitude to my teachers Mr. Vashram Barad and Mr. Nishant Shah who taught me not only as a student of academic subjects but as a student of life.

Here at CSU, I would like to express my deepest gratitude to my adviser Christine Chiu for all the scientific discussions. I would also like to thank my committee members Chris Kummerow and Shantanu Jathar for all the valuable inputs that improved the quality of my thesis. A very special thanks to a very kind person, Kevin for sharing with me the example machine learning code and all the helpful discussions on machine learning methods throughout the last 1.5 years. A big thank you to Joe who generously offered me rides in my first year and all our interesting conversations on the world.

I have also been very fortunate of having friends who were always a call away whenever I needed them. I am very grateful for having you all – Sagar, Rudra, Drashti, Mihir, Kaxan, Kathan, Sachin, and Preet.

TABLE OF CONTENTS

CHAPTER 1: INTRODUCTION

1.1 Background

Water vapor is the most fascinating constituent of the earth-atmosphere system. With its interwoven thermodynamic, radiative, and dynamic influence, water vapor lies at the heart of a wide range of atmospheric processes governing the weather and climate of the planet. It is not only the most dominant greenhouse gas (Kiehl & Trenberth, 1997), water vapor is also a dominant feedback variable constituting a strong positive radiative feedback that amplifies CO_2-caused global warming and also affects the global climate sensitivity to CO_2 perturbations (Held & Soden, 2000).

Water vapor manifests its strongest control on atmospheric processes by modulating the energy flows of the earth system. It governs the distribution of energy between the surface, atmosphere, and space through the exchange of latent heat from the surface in form of evaporation and condensation in the atmosphere (Allan, 2012). The latent heat of water vapor also accounts for roughly half the poleward, and most of the upward heat transport (Sherwood et al., 2010). The thermodynamic effects of water vapor in the lower troposphere influence the formation of clouds. With the water vapor dominating the net radiative cooling of the troposphere, it also determines the strength and depth of convection, especially in the tropics (Stevens et al., 2017). As a result, the thermodynamics of the water vapor couples with the radiative effects and plays an active role in the dynamical processes that shape the global circulation of the atmosphere (Schneider et al., 2010).

Water vapor, with its rich infrared (IR) absorption spectrum, regulates the radiative energy flows in both the longwave and shortwave portions of the electromagnetic spectrum. Kim et al. (2022) show that the shortwave absorption by water vapor shapes the mean climate patterns of sea surface temperature (SST) and also as a result, imposes a significant energy constraint on the global-mean precipitation. In the longwave, the moisture profile of the troposphere is found to act as an important control on the variability of outgoing longwave radiation (OLR) to space which is the primary cooling mechanism of the earth-atmosphere system (Allan et al., 1999). Further, it is also found that even though the stratosphere contains very low concentrations of water vapor, it plays an important role in setting the surface temperatures and its trend on the decadal timescales (Forster & Shine, 1999; Forster & Shine, 2002; Solomon et al., 2010; Dessler et al., 2013).

Advancing the observational capacity to understand the variability of water vapor by better representing the four-dimensional distribution of water vapor is thus essential to improve the knowledge and prediction of all these key atmospheric processes. Satellite observations, with its global coverage and high spatial resolution in low-earth orbit, and unprecedented temporal resolution in the geostationary orbit, are the backbone to the continuous effort of measuring the time evolution of horizontal and vertical structures of the atmospheric fields. Improved data assimilation capacity with the availability of large volumes of satellite observations has not only improved the quality of global reanalysis dataset with better general circulation model (GCM) outputs (Fasullo & Trenberth, 2008; Trenberth et al., 2009), but the prediction skill of numerical weather predictions (NWP) has also enhanced manifolds (Bauer et al., 2015; Menzel et al., 2018).

Commonly used passive remote sensing satellite instruments record upwelling radiances in the absorption bands of both, shortwave (SW) and longwave (LW) portions of infrared and in the microwave (MW) regions of the electromagnetic spectrum. The radiation field in these spectral bands is absorbed by various atmospheric molecules such as water vapor, carbon dioxide, ozone, nitrous oxide, oxygen, etc. The subsequent emission from these absorbers as a function of atmospheric temperature characterizes the spectral radiance received by the satellite instrument at the top-of-atmosphere. The absorption and emission properties of the atmospheric constituents are then utilized to infer the profiles of atmospheric state-variables like water vapor concentration and temperature.

The Moderate Resolution Imaging Spectroradiometer (MODIS) has water vapor channels in the water vapor absorption band around 0.94 µm in near-infrared spectral region. MODIS is an imager that retrieves the column integrated water vapor (IWV) amounts by making observations of the reflected solar radiation in near-infrared along with the use of atmospheric window bands at 0.86 and 1.24 µm (King, 1992; King et al., 2003). Column integrated quantification of water (IWV) is crucial for studies focusing on high-impact weather phenomena like atmospheric rivers and other extreme precipitation events for their description of moisture availability and transport (Wick et al., 2013; Rutz et al., 2019; de Vries, 2021). In the longwave, commonly used satellite channels rely on absorption and emission in the short wavelength and long wavelength side of the thermal-infrared v_2 vibrational band centered at 6.3 µm, or in the short wavelength side of the rotational band between 17 to 18.6 µm (Smith et al., 1999). The microwave radiometers exploit the absorption lines produced by the electric field interaction of water molecules at around 22.3 GHz, which is a weak absorption band, and the stronger absorption band at 183.3 GHz (Goldberg & Weng, 2006).

Infrared instruments, owing to their ability to sample absorption lines of varying optical depths at the hyperspectral resolution, provide a large number of unique weighting functions of various strengths when compared to microwave instruments (Wulfmeyer et al., 2015). As a result, infrared instruments provide better vertical-sounding resolution, and consequently, the IR information content is typically 2-3 times larger than MW (Löhnert et al., 2009). The prime advantage of microwave sounders is their ability to observe in the presence of nonprecipitating clouds which significantly extends the number of observations that can be assimilated to the NWP model over the oceans. On the other hand, infrared sounders can be deployed in the geostationary orbit (GEO) and provide unparalleled temporal resolution crucial for weather forecasting and nowcasting applications (Schmit et al., 2009). Microwave remote sensing is restricted to low-earth orbits (LEO) because in order to achieve the required signal-to-noise ratio (SNR) and practical integration time for weakly emitted MW signal from the earth at GEO flight level would require a very large antenna (Thies & Bendix, 2011; Wulfmeyer et al., 2015). The new technological development in microwave instrumentation aims to solve this and it is also expected to have hyperspectral observation capability for improved vertical resolution (Blackwell et al., 2011).

The most positive impact of satellite observations is the strengthened capacity for the timely issuance of high-quality short-range forecasts (Joo et al., 2013). However, the performance of the existing suite of operational satellites is still deficient when it comes to profiling the lower part of the troposphere (Crevoisier et al., 2014). Low-level, near-surface profiling in the thermal-IR spectrum gets challenging due to the thermal emissions of the earth's surface. Because of similar brightness temperatures (BT) from surface and near-surface atmospheric emissions, sounders require large-enough information content to accurately contrast surface and atmospheric emissions. Microwave sounders are not affected by this difficulty, particularly over the ocean, because of low emissivity. However, both, infrared and microwave sounders struggle over land from the uncertainties in the surface emissivity and information on soil moisture. With improvements in the radiometric accuracy of observing instruments and efforts towards improving simultaneous retrievals of surface emissivity, the hyperspectral instruments are expected to reliably resolve the near-surface radiances (Zhou et al., 2011; Capelle et al., 2012). However, the progress is limited.

Future American and European missions planned by both, NOAA and EUMETSAT, have proposed hyperspectral infrared sounders preferably in the geostationary orbit with an important objective of better representing the boundary layer processes in the NWP models (Adkins et al., 2021; Holmlund et al., 2021). The induction of a geostationary hyperspectral infrared sounder in operational use will be especially beneficial for the prediction of high-intensity storms (Smith et al., 2020; Wang et al., 2021). The environment leading to severe storms is associated with high temporal and spatial variations in the lower-tropospheric moisture (Di et al., 2021). With improved vertical resolution from hyperspectral observations and a higher sampling rate in the time domain, crucial information regarding the water vapor distribution and instability of the pre-convective environments will lead to substantial improvement in nowcasting and short-term forecasts of severe weather (Li et al., 2012). The hydrological cycle is intimately linked to water vapor available in the lower troposphere providing the main resource for precipitation in all weather systems (Trenberth et al., 2005). Precipitation picks up exponentially with the increase in column relative humidity (Bretherton et al., 2004; Sherwood et al., 2010). The distribution of total column water vapor which is concentrated in the first few kilometers in the lower troposphere has a very influential control over radiative fluxes that set the surface heat budget (Zhang et al., 2006; Allan, 2012; Stevens et al., 2017). With the warming of the climate, the amount of moisture in the atmosphere with the Clausius-Clapeyron relation is expected to rise faster than the total precipitation amount which is governed by the surface heat budget through evaporation (Trenberth et al., 2003). As a result, the improvement in the quality of observations will bring high value in understanding how precipitation changes with trends of moisture availability. Further, the climate modeling community will also benefit in narrowing the largest uncertainty introduced by clouds as Vial et al., (2017) note the important role of humidity variation in determining the cloud amount.

1.2 Research in this thesis

The central question in the remote sensing of a physical system is – given a set of radiation measurements, what can be deduced about the physical state of the system (Isaacs et al., 1986). The quality of this deduction or retrieval of the physical state depends on the accuracy of the forward and inverse modeling employed in carrying out this inference. The radiance recorded by a passive remote sensing instrument is a dependent quantity of a number of independent state variables, primarily – temperature, pressure, and the atmospheric constituents that absorb, emit, and scatter the radiation such as gas molecules, clouds, and aerosol. The mapping of the dependent variable on the independent state variables is expressed by the wavelength dependent radiative transfer processes on the prescribed atmospheric path. However, the process of retrieving the physical state of the system by the means of remote sensing is fundamentally an ill-posed problem, i.e., for the same value of the dependent variable there exist a non-unique and non-continuous set of independent variables. The inversion of the dependent variable means approximating the values of the independent variables, which in the context of remote sensing is the retrieval of the state variables. This process is known as inverse modeling. Crucial to solving the inverse problem is forward modeling. It is the process of constraining the ill-posed and ill-conditioned relationship of the dependent variable on independent variables with the use of a-priori knowledge of the physical state of the system. An a-priori for remote sensing purposes can be a set of climatological profiles of various atmospheric parameters or in the case of the NWP model, it can be the best estimate of the model state from the previous analysis step. Using this a-priori information, the forward model simulates the dependent variable by solving the radiative transfer equation. The simulated values are then compared with the observed values to iteratively update the a-priori until they converge. The retrieved variables or observed radiance are similarly assimilated in the NWP model by optimally adjusting the model-state variables that match with the observed values to provide the best estimate of the state of the physical system.

The radiative transfer models commonly used by the remote sensing and data assimilation community to solve the forward and inverse problems are, Community Radiative Transfer Model (CRTM) and Radiative Transfer for TOVS (RTTOV). These are fast and accurate one-dimensional radiative transfer models for the simulation of top-of-atmosphere visible, infrared, and microwave radiances observed by downward viewing space-borne passive sensors (Liu et al., 2012; Saunders et al., 2017). They also contain K-matrix (Jacobian) models for solving inverse problems. The value of these models in their application to operational usage is their ability to efficiently and accurately solve the radiative transfer equation.

1.2.1 Calculation of gas absorption in radiative transfer models

Various methods are used for accounting the gas absorption in radiative transfer models. The most basic and simple method is look-up tables. It lists a precalculated set of near-monochromatic absorption coefficients for a range of temperature and pressure for a specified spectral interval (Strow et al., 1996; Buehler et al., 2011). This approach strictly limits the flexibility as calculations can only be carried out for precalculated spectral intervals. A more flexible approach that retains its accuracy and speed is the technique called Optimal Spectral Sampling (OSS). This method optimally selects wavelengths in the bandwidth of a sensor's channel and appropriately weights the monochromatic spectral points contributing to the channel (Moncet et al., 2004). Using a similar approach principal component (PC) based fast model PCRTM (Principal Component Radiative Transfer Model) weights the monochromatic spectral points using the PC scores (Liu et al., 2005). These methods are mainly focused on simulating remote sensing instruments' channel radiances. The radiative transfer models used in general circulation models also require efficient calculation of gas absorption for computing broadband fluxes. Rapid Radiative Transfer Model for GCM (RRTMG) is a commonly used radiative transfer model in many GCMs. It uses an innovative way of reducing the required number of radiative transfer calculations by using the correlated *k*-distribution (CKD) method (Mlawer et al., 1997). It exploits the fact that the absorption spectrum varies irregularly but in a given absorption band multiple wavelengths share absorption coefficients of the same magnitude. By grouping all such wavelengths, the CKD method then rearranges them to monotonically increasing value of the absorption coefficient. This results in a cumulative density function (CDF) that represent the occurrence frequency of a given absorption coefficient value. The integration over the CDF gives the broadband gas absorption contribution over the specified spectral interval. The process of calculating these CDFs is carried out for a wide range of environmental conditions that accounts for the change in absorption coefficient values and line shapes of the spectrum.

The regression-based procedures used in CRTM and RTTOV are based on the same method originally developed by McMillin & Fleming (1976). The method was restricted to gases having a constant mixing ratio, for example, carbon dioxide, and for a slant path defined by a single zenith angle. With subsequent developments, the original method was improved to incorporate calculations at an arbitrary zenith angle (Fleming & McMillin, 1977), and further for gases with variable mixing ratios, for example, water vapor (McMillin et al., 1979). Based on these methods, the U.S. National Environmental Satellite, Data, and Information Service (NESDIS) implemented a fast radiative transfer model (Weinreb et al., 1981) for operational sounders. Later Eyre & Woolf (1988) built upon the original methods to simultaneously handle the absorption from gases with fixed and variable mixing ratios for microwave region. At its core, these methods regress channel transmittance profiles with the profiles of various environmental predictors such as temperature, pressure, absorber concentration, etc., to obtain regression coefficients. With the methods described in McMillin et al. (1979) and Eyre & Woolf (1988), the European Centre for Medium-Range Weather Forecasts (ECMWF) developed the fast radiative transfer model for satellite sounding systems and for data assimilation in NWP models (Eyre, 1991). A significant shift in the methodology of implementing fast gas absorption came with the introduction of OPTRAN – Optical Path Transmittance (McMillin et al., 1995a; McMillin et al., 1995b). In the earlier methods, the atmosphere was stratified in the vertical coordinate using a fixed set of pressure levels – this approach was also known as Pressure Level Optical Depth (PLOD). OPTRAN, on the other hand, stratifies the atmosphere with the layers defined by a fixed set of absorber amounts. The primary reason for this design choice was to improve the variable gas predictions by making the effect of variable gas concentration on transmittance values implicit in the layering scheme on which the regression coefficients are calculated. This marked the beginning of independent fast radiative transfer model development as the American centers adopted OPTRAN in their operational models and the European counterparts continued using the PLOD approach. However, the subsequent developments in both American and European operational models continued to share a resemblance. For example, the concept of effective transmittance and correction terms to sum up the influence of multiple gases in the same channel were introduced around the same time in RTTOV and OPTRAN (Saunders et al., 2006; McMillin et al., 2006). The same also introduced separate treatments of water vapor lines and continuum.

With the current version of CRTM, the American centers continue using the further developed version of OPTRAN – Compact-OPTRAN, named for its efficient memory utilization due to the lesser number of coefficients (Liu et al., 2012). However, apart from Compact-OPTRAN, which is called ODAS (Optical Depth on Absorber Space) in CRTM, it also implements a method based on PLOD known as ODPS (Optical Depth on Pressure Space), while RTTOV continues to use regression methods based on PLOD approach (Hocking et al., 2021).

However, with ODAS and ODPS, the ability to simulate satellite radiances in CRTM is limited to specific channels for which the ODAS and ODPS regression coefficients are generated. As a result, for any applications using satellite observations in new channels, ODAS and ODPS coefficients need to be regenerated by performing new line-by-line radiative transfer calculations and regression analyses, which can pose a great challenge for CRTM users.

1.2.2 New machine-learning method for calculating gas absorption

Artificial intelligence techniques are increasingly being adopted in the atmospheric and climate science community, particularly the machine learning (ML) methods are commonly used in numerical modeling to represent various sub-grid processes by simple parametric relations (Brenowitz & Bretherton, 2018; O'Gorman & Dwyer, 2018; Rasp et al., 2018). Also, in the remote sensing and data assimilation community, AI techniques are being exploited to tackle data-intensive tasks (Rasp & Lerch, 2018; Boukabara et al., 2019). Unlike the parameterization of sub-grid processes in dynamical models, the radiative transfer processes are well known but the exact solution of the radiative transfer equation remains the most expensive and time-consuming, and therefore not feasible for operational purposes. As a result, the use of machine learning techniques for radiative transfer purposes is focused on implementing parametric computations that are more efficient than the solutions from exact formulations (Ukkonen et al., 2020). Previous studies focused on using machine-learning techniques for radiative transfer purposes are focused on calculating broadband shortwave and longwave fluxes for radiation computations in the general circulation models (Chevallier et al., 1998, 2000; Krasnopolsky et al., 2008). Generally, these methods train neural networks (NN) to emulate the correlated *k*-distribution parameterization of

RRTMG (Veerman et al., 2021). To the best of our knowledge, at the time of writing this thesis, there is only one study focused on applying machine learning methods for gas absorption calculations in the forward modeling of satellite radiances. The recent study carried out by Stegmann et al. (2022), is focused on evaluating the feasibility of neural networks for the prediction of channel transmittance profiles using an example of two infrared channels of Visible Infrared Imaging Radiometer Suite (VIIRS). The design of the study proposed by Stegmann et a. (2022) is focused on replacing the ODAS and ODPS regression-based methods in CRTM.

In the present study, we aim to explore the use of machine learning techniques to emulate line-by-line optical depths and thus transmittance, replacing the regression-based approach used in CRTM. This helps facilitate the remote sensing community in designing the spectral characteristics of new sensors. With the capability of simulating satellite radiances using CRTM for hypothetical sensors, a better spectral design can be selected for future sensors from the comparison of a range of spectral intervals. We also demonstrate the use of our method in calculating channel-convolved quantities for their application in CRTM for a new water-vapor channel in thermal infrared on the proposed Geostationary Extended Observations (GeoXO) mission by NOAA. The objective of our study is to explore the usefulness and possible challenges associated with line-by-line emulation of layer optical depths which can be later convolved with a given sensor response function and used by CRTM.

1.3 Outline of the thesis

The thesis is organized as follows. In Chapter 2, we start by briefly discussing the theoretical background of computing gas absorption optical depths. After providing the basic spectral information about the infrared channel used in this thesis, we discuss the gas absorption in this channel using a standard atmospheric profile. Additionally, the atmospheric absorption characteristics of the channel are briefly explained with the calculations of the weighting function and its comparison with existing thermal-infrared water vapor channels. Further, the conventional methods of gas absorption parameterization used in the current operational forward radiative transfer models are described. We then provide an overview of our machine learning based method of gas absorption calculations. The methodology of preparing the training, validation, and testing data is explained with the design of the neural networks trained to predict line-by-line layer optical depth.

In Chapter 3, the performance of the trained neural networks is evaluated with a discussion on the sources of prediction errors. Further, the prediction skill for channel transmittance values is also discussed. The error statistics of the trained neural networks are summarized.

In the final Chapter 4, the summary of the work presented in this thesis is provided, and key conclusions are briefly discussed with thoughts on future work.

CHAPTER 2: METHODOLOGY

2.1 Theoretical background on computing gas absorption optical depths

Calculations of optical depths require spectroscopic information of a given spectral region and information on the environmental conditions – particularly, pressure, temperature, absorber concentration, and path length. HITRAN (High Resolution Transmission Molecular Absorption Database) provides spectroscopic parameters such as line-by-line (as a function of wavenumber) transition intensity (S – units, $cm^{-1}/(molecule/cm^2)$) for gas molecules at the reference condition of 296 K and 1 atmospheric pressure (Rothman et al., 2013). With the use of temperature and pressure dependence spectral parameters of each gas molecule also provided in the HITRAN database, the reference values of S are scaled to pressure and temperature values of interest. The Voigt line-shape function accounts for the effect of pressure and temperature on the broadening of line shapes. For any given wavenumber (v), multiplying the line intensity value S with line-shape function (V) gives the value of absorption cross-section (σ – units, $cm^2/molecule$) as:

$$\sigma(v) = S(v) \cdot V(v). \tag{2.1}$$

Once we have the absorption cross-section for a given gas molecule at the given environmental conditions, the volume absorption coefficient (β with units of cm^{-1}) can be calculated by:

$$\beta = \sigma \cdot \rho, \tag{2.2}$$

where ρ is the density of absorbing material expressed in $molecules/cm^3$ for gases. Assuming a homogeneous absorbing medium, β provides the measure of absorption as a function of path length, denoted as l. At last, the optical depth (τ) of a given gas species can be calculated by:

$$\tau = \beta \cdot l. \tag{2.3}$$

Optical depth is a unitless quantity expressing the opacity of an absorbing medium. The fraction of incident electromagnetic radiation that is transmitted through an absorbing medium is then given as:

$$\mathcal{T} = e^{-\tau}, \tag{2.4}$$

where the transmittance, $\mathcal{T}$, is the quantity that is generally used in the radiative transfer equations to account for the gas absorption. From the above discussion, we can recognize that the physical variables controlling gaseous absorption are pressure, temperature, and absorber amount. The process of calculating optical depth or transmittance is summarized in the flow chart below.

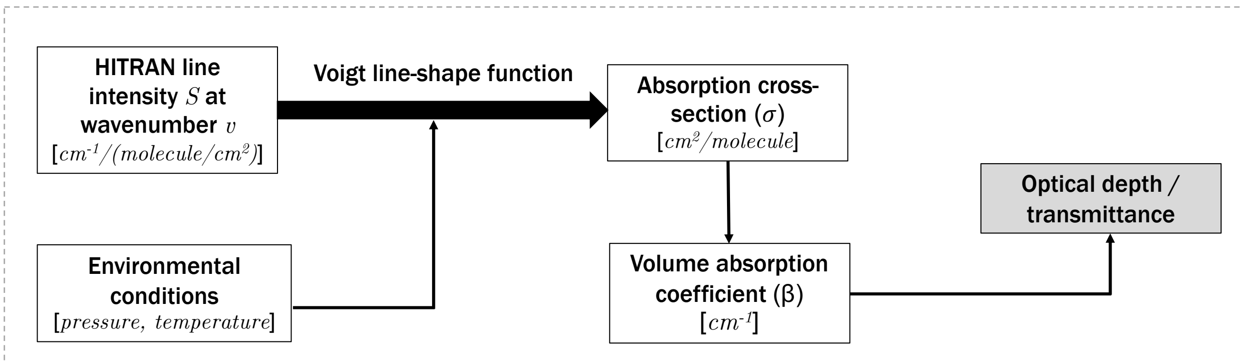

Figure 2.1. Flowchart explaining the process of optical depth / transmittance calculation.

2.2 Spectral characteristics of the channel

2.2.1 Basic spectral information of the channel

The new GeoXO water-vapor channel with a central wavelength of 5.15 µm is a thermal infrared channel aimed at retrieving water-vapor information in the lower troposphere. The channel is located on the short wavelength side of the v_2 (bending mode) fundamental vibration band at 6.3 µm. The radiation in this channel is influenced by the earth's emission and shortwave radiation, but the impact of Rayleigh and aerosol scattering on this channel is small. The spectral detail of this channel is outlined in Table 2.1.

Table 2.1. Spectral information of the new GeoXO water-vapor channel.

Parameter	Value
Beginning wavelength (wavenumber)	4.93909 μm (2024.66 cm^{-1})
Ending wavelength (wavenumber)	5.36091 μm (1865.35 cm^{-1})
Number of spectral points	302
Spectral resolution	0.0014 μm

The Spectral Response Function (SRF) describes the relative sensitivity of the observing instrument to incident radiant power as a function of wavelength. As shown in Figure 2.2, the new GeoXO water vapor channel has an SRF that peaks at the central wavelength of 5.15 μm with wings of the channel having zero relative response.

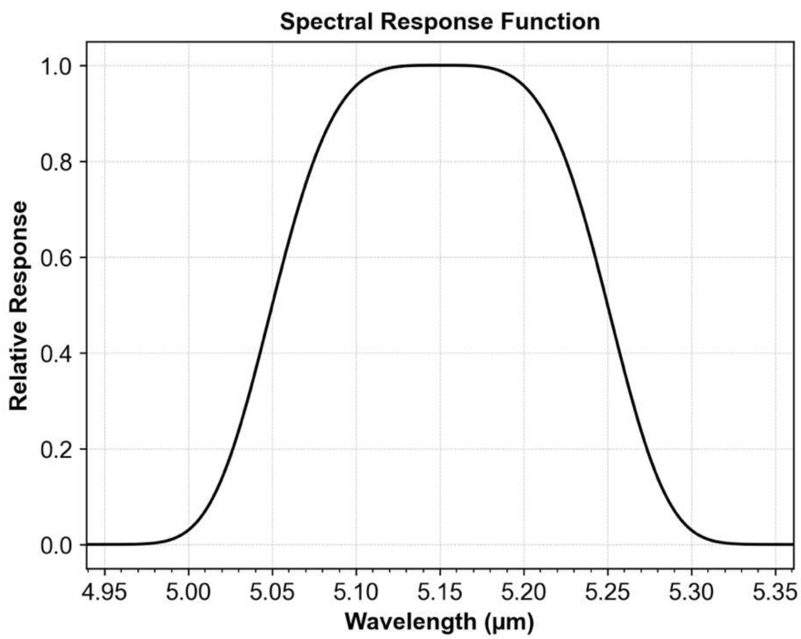

Figure 2.2. The spectral response function of the new GeoXO water vapor channel.

2.2.2 Gas absorption in the channel

From the HITRAN database, we know that six gas absorbers have transition lines in the spectral region of the new GeoXO channel between 4.94 – 5.36 μm. These gas absorbers are water vapor (H_2O), carbon dioxide (CO_2), ozone (O_3), nitrous oxide (N_2O), carbon monoxide (CO), and methane (CH_4). To understand the gas absorption in the atmosphere, we ran MonoRTM (Clough et al., 2005) using the U.S. Standard Atmosphere profile. The details of MonoRTM are described later in Section 2.4.1. The total layer optical depth due to all six gas absorbers are shown in Figure 2.3. As explained in Section 2.1, the layer optical depth depends on the absorption coefficient at the given wavenumber. We calculated the absorption coefficients associated with the gas molecules using HAPI – the HITRAN Application Programming Interface (Kochanov et al., 2016). The absorption coefficient spectrum is shown in Figure 2.5. HAPI is a Python-based library developed by the HITRAN working group to facilitate the calculations of various spectroscopic quantities using the HITRAN database. HAPI uses spectral parameters from the HITRAN database and computes the absorption coefficient by scaling the reference line-transition intensity values (S) to the input pressure and temperature values. We used the Voigt line-shape function for the calculations of absorption cross-sections (σ).

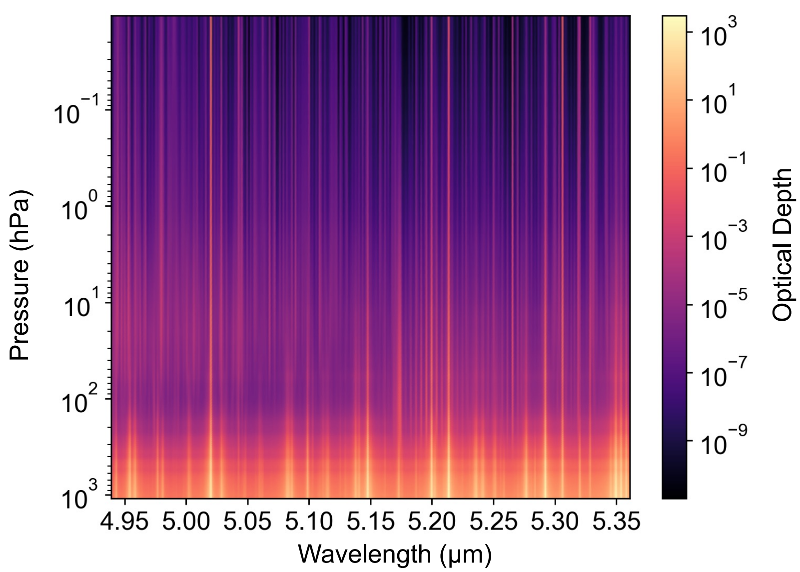

Figure 2.3. Line-by-line layer optical depth calculated using the U.S. Standard Atmosphere profile over the spectral band of the new GeoXO water vapor channel.

Water vapor is the primary and dominant absorber in the channel. However, water vapor is dominant only from the surface up to 200 hPa (~13–14 km). In the upper atmosphere with pressures less than 200 hPa, carbon dioxide and ozone have the largest contribution to the total layer optical depth (Figures 2.4(b) and 2.4(c)). It can be attributed to a lower concentration of water vapor and an increase in the ozone concentration. However, from Figure 2.5, we can see that it is largely because the absorption coefficient values of ozone and carbon dioxide become comparable to that of water vapor in the upper atmosphere. Since the upper atmosphere does not have appreciable amounts of water vapor present, the largest contribution to the total optical depth comes from ozone and carbon dioxide except in the strongly absorbing water vapor wavelengths.

The absorption spectrum shown in Figure 2.5 also illustrates the impact of pressure broadening on the line shape. In the lower pressures of the upper atmosphere, the line shapes are remarkably narrow and absorption coefficient values change sharply compared to the surface spectrum. As a result, the layer optical depth values in the upper atmosphere change rapidly as a function of wavelength.

Other gas molecules such as nitrous oxide, carbon monoxide, and methane have only a few absorbing wavelengths and are located in the wings of the channel. As can be seen in Figures 2.4 (d) and (e), these absorbers have negligible impact on the radiance received by the satellite since wavelengths associated with their absorption lie in the wings of the channel where the SRF is zero. Methane (Figure 2.4f) shows absorption for pressures less than 1 hPa with only one wavelength (~ 5.18 μm) near the center of the channel. However, this wavelength contributes less than 10% to the total optical depth, and as a result, the impact of methane can also be considered negligible.

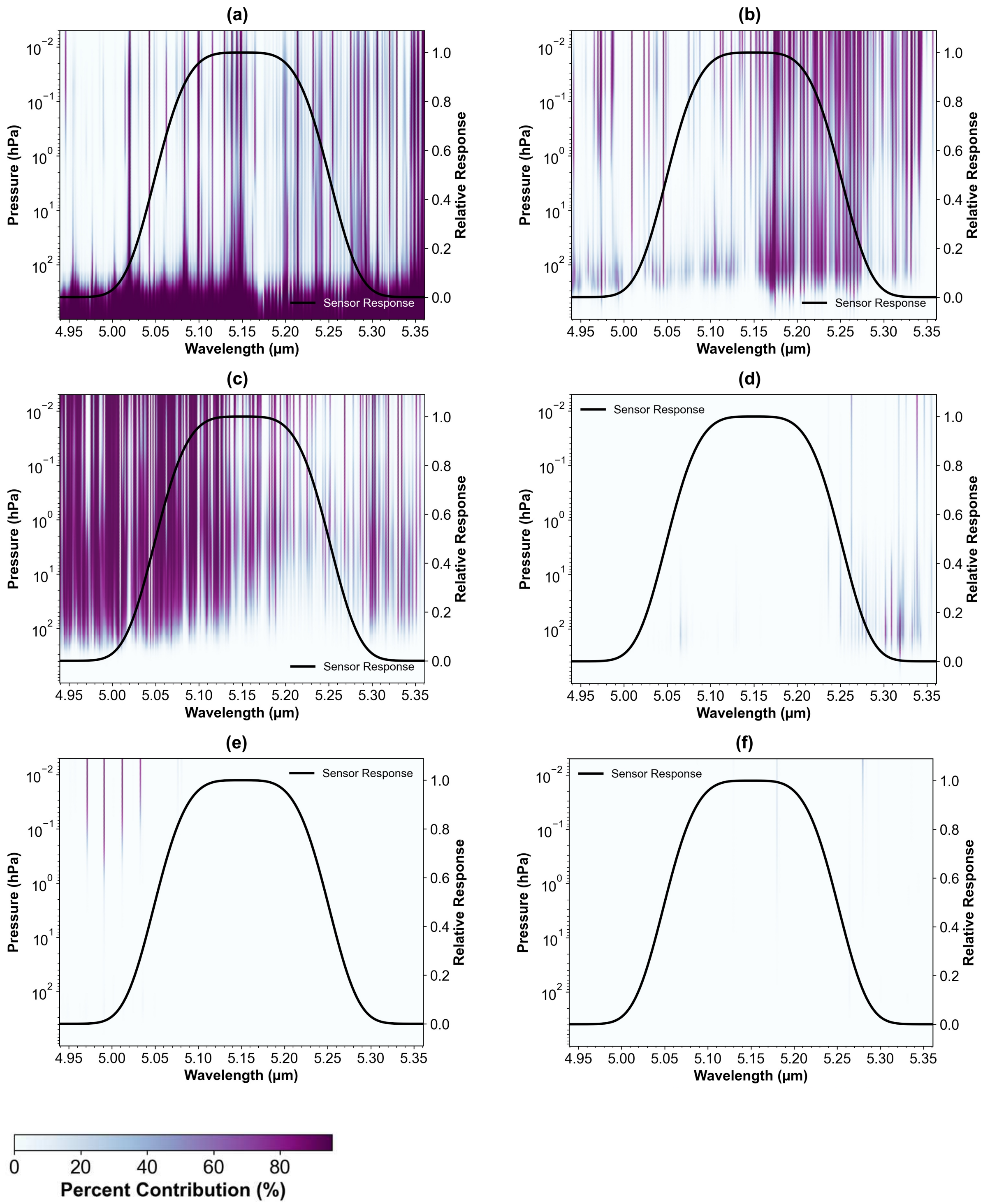

Figure 2.4. Fractional contribution to total layer optical depth from (a) water vapor (b) carbon dioxide, (c) ozone, (d) nitrous oxide, (e) carbon monoxide, and (f) methane. The spectral layer optical depth profiles are overlaid with the spectral response function of the new GeoXO water vapor channel.

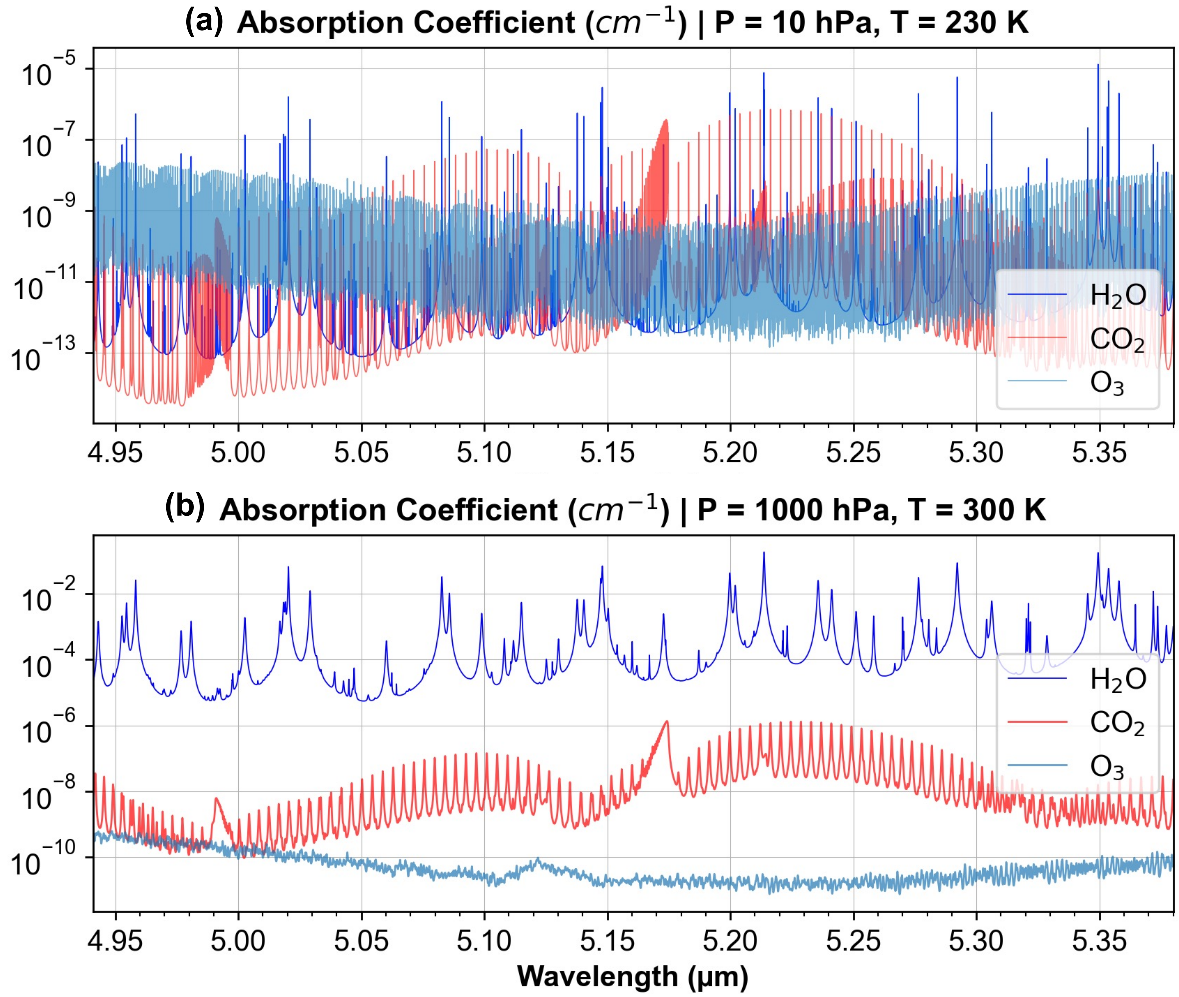

Figure 2.5. Absorption coefficient spectrum of water vapor (H_2O), carbon dioxide (CO_2), and ozone (O_3), for (a) the atmosphere at 10 hPa pressure and 230 K temperature, and (b) for the atmosphere at 1000 hPa pressure and 300 K temperature.

2.2.3 Absorption in the atmosphere

An important aspect of selecting the spectral interval for a channel is to understand where the radiation received by the satellite instruments comes from in the atmosphere. This understanding provides the basis for designing the application of the channel. Calculating the weighting functions of the channel as a function of pressure or altitude provides this essential information. Weighting functions are derivatives of transmittance with respect to pressure or height and it estimates the relative contribution of each atmospheric layer to the radiation received by the satellite instrument.

The spectral intervals of the channels that are used for sounding of atmospheric variables are generally selected in the wings of the absorption bands because, in the center of the absorption band, the absorption is so strong that radiation from only the uppermost layers of the atmosphere can reach the instrument. As we move towards the wings of the absorption band the absorption strength progressively decreases, allowing the radiation from increasingly lower layers in the atmosphere to reach the instrument.

The vibration mode (v_2) absorption band centered at 6.3 μm is commonly utilized to retrieve water vapor profiles in the IR spectrum. The Advanced Baseline Imager (ABI) on the GOES series has three channels centered around 6.19, 6.95, and 7.34 μm for observing respectively the upper-level, mid-level, and lower-level water vapor. The new GeoXO water vapor channel centered at 5.15 μm is further away from the absorption band center, providing water vapor information from lower in the atmosphere. The profiles of layer-to-space optical depth, transmittance, and weighting functions of the new GeoXO water vapor channel are shown in Figure 2.6. Its weighting function is compared with the weighting functions of ABI water vapor channels and shown in Figure 2.7.

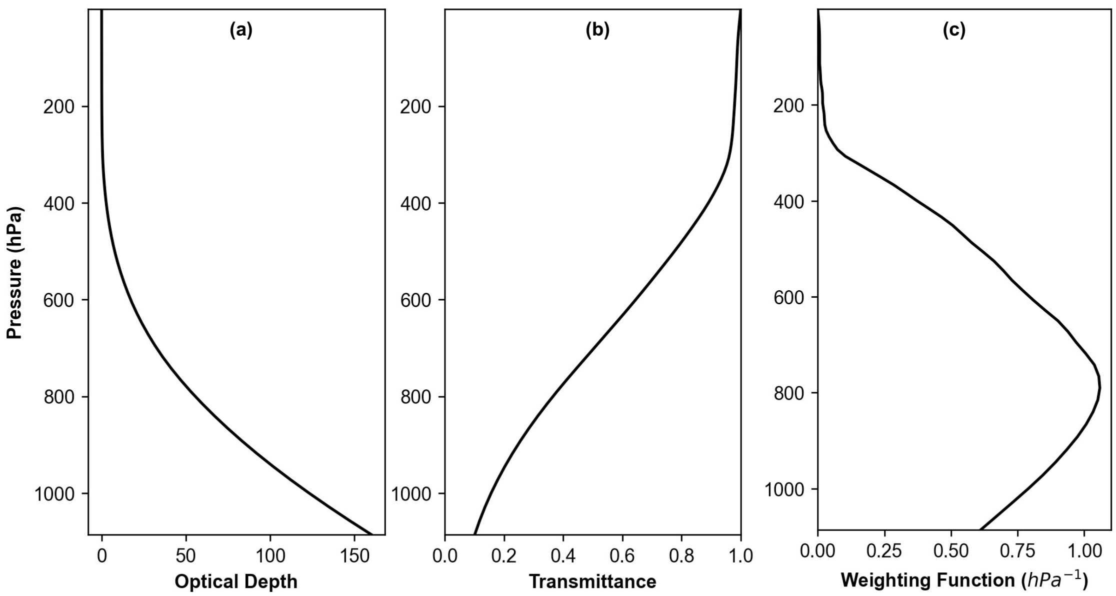

Figure 2.6. Profiles of (a) layer-to-space optical depth (b) layer-to-space transmittance, and (c) weighting function for the new GeoXO water vapor channel calculated using the U.S. Standard Atmosphere profile.

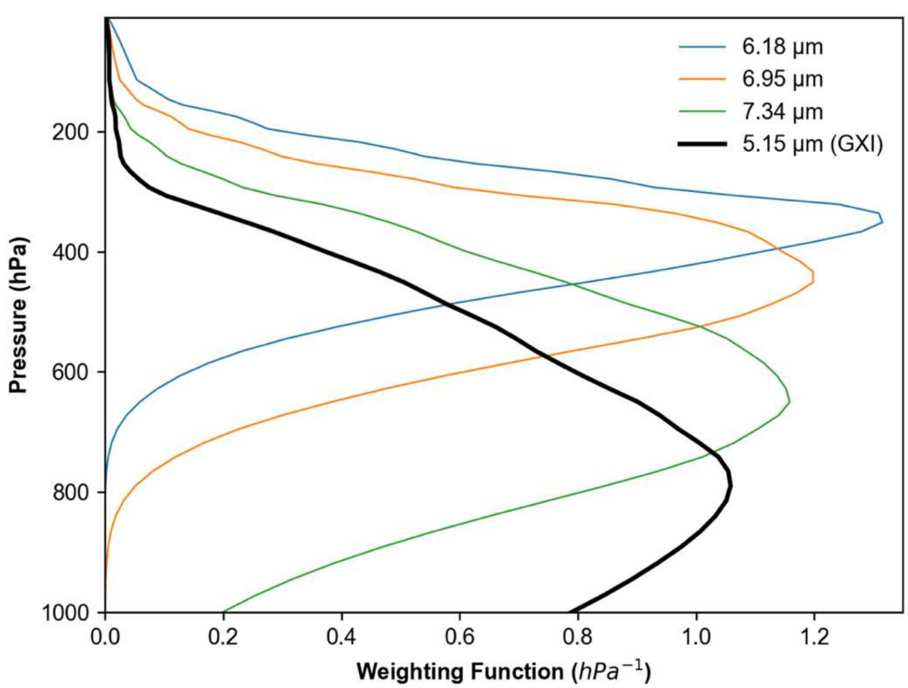

Figure 2.7. Weighting functions for water vapor channels of GOES-R ABI at wavelengths of 6.18 μm, 6.95 μm, and 7.34 μm with the new GeoXO water vapor channel at 5.15 μm (denoted by GXI), using the U.S. Standard Atmosphere profile.

2.3 Gas absorption parameterization in radiative transfer models

As shown in Figure 2.5, gas absorption lines have a complex structure and thus the most precise method for calculating gas absorption is summing the influence of every spectral line and non-resonant absorption process for each contributing line. Since these calculations are computationally expensive, gas absorptions are often parameterized using various techniques introduced in Section 1.2.1. In this section, we detail the regression-based parameterizations available in CRTM, to provide a context for our machine-learning-based method.

2.3.1 Conventional methods of gas absorption parameterization

Figure 2.8 illustrates how the existing regression coefficients of gas absorption in CRTM are derived. First, monochromatic optical depth or transmittance values are calculated using a line-by-line model using a set of atmospheric profiles representing diverse atmospheric conditions. In the second step, the monochromatic values are convolved with SRF to get transmittance profiles for the specific channel of the sensor. Lastly, the channel-specific regression coefficients are determined using the channel transmittance computed in the second step as predictands and atmospheric variables – pressure, temperature, and absorber concentration as predictors. Once the channel-specific regression coefficients are computed, they are used as weights in the fast gas absorption model to predict channel transmittance for a given input of atmospheric profile.

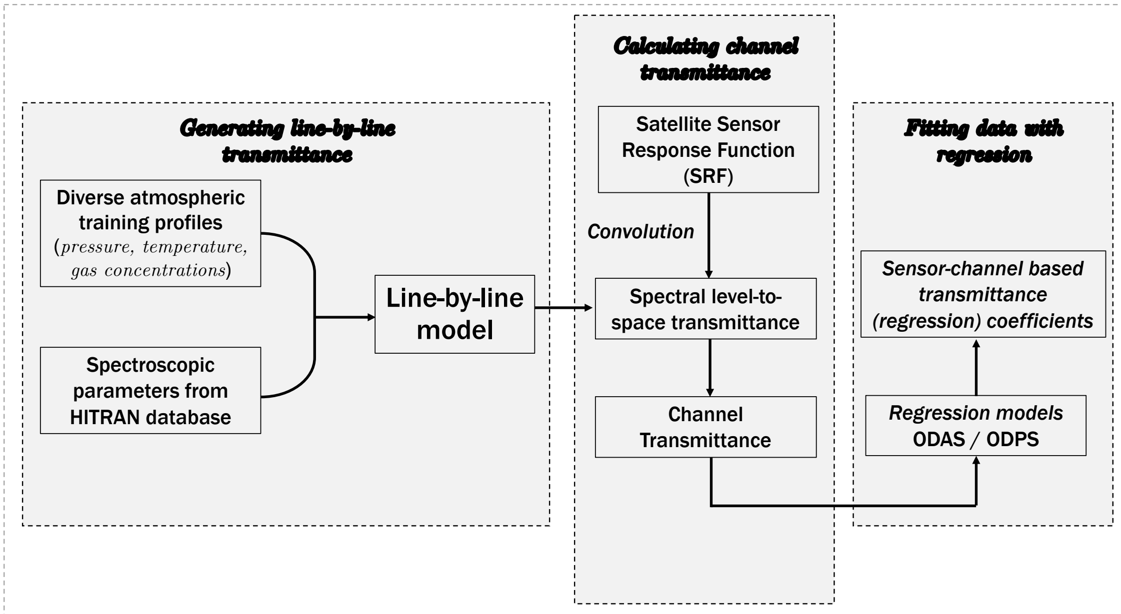

Figure 2.8. Flowchart summarizing the workflow of CRTM Coefficient Generation Package. Adapted from Stegmann, (2020).

CRTM contains two regression algorithms, ODPS and ODAS (Chen et al., 2012; Liu et al., 2012). Structurally both algorithms are similar and differ conceptually only by how they stratify the atmosphere in the vertical coordinate. The regression equations of ODPS predict channel transmittance on layers defined by a fixed grid of pressure levels, while ODAS makes predictions on layers of fixed absorber amounts. However, both algorithms output values on the common grid on which the input atmospheric profiles are supplied. More details about these two algorithms are briefly discussed next.

2.3.2 Optical Depth on Pressure Space (ODPS)

ODPS was originally developed for gases having a constant mixing ratio. The central idea is that at a given pressure level in the atmosphere, the layer-to-space transmittance for a well-mixed absorbing gas is proportional to the atmospheric pressure and varies with the temperature profile (McMillin & Fleming, 1976). ODPS calculates regression coefficients by slicing the atmosphere into a grid of constant pressures defined by a fixed set of pressure levels. The most commonly used atmospheric layering scheme is designed by the AIRS Science Team and is explained in Hannon et al. (1996) and Strow et al. (2003). The 101 pressure levels spanning from 1100 hPa to 0.005 hPa stratifies the atmosphere in 100 layers. Using the channel optical depth values from line-by-line calculations as predictand, ODPS calculates regression coefficients $c_{i,j}$ using the following regression equation (Chen et al., 2010):

$$d_i - d_{i-1} = \sum_{j=1}^{N_p} c_{i,j} X_{i,j} \tag{2.5}$$

where, d_i is the level-to-space optical depth from level i, N_p is the number of predictors, and $X_{i,j}$ is j^{th} predictor for i^{th} layer (e.g., pressure, temperature, and gas concentrations). Thus, the regression coefficient is derived basically by relating layer optical depths ($d_i - d_{i-1}$) to atmospheric variables X. The functional forms of predictors are carried out by trial and error and are continuously updated. A list of functional forms of ODPS predictors can be found in Matricardi et al. (2004) and Hocking et al. (2021). Although originally developed for well-mixed gases, the modern ODPS can incorporate multiple variable gases (Chen et al., 2012).

2.3.2 Optical Depth on Absorber Space (ODAS)

The concept of calculating optical depth in absorber space instead of pressure space was first introduced by McMillin et al. (1979). The framework for calculating optical depths on an absorber space was adopted because, unlike well-mixed gases, the absorber amounts of variable gases (e.g., water vapor) are not fixed for a fixed pressure level, and thus the relation between absorber amount and pressure can vary significantly with different atmospheres (McMillin et al., 1995a). Since transmittance depends strongly on absorber amount, ODAS defines its vertical layering with a constant path integrated absorber amount such that the layer optical paths are always constant across a layer (Hannon et al., 1996), which improves the gas absorption parameterization for variable gases.

However, with this approach, each absorbing gas has its own layering grid. The maximum and minimum values for the fixed grids for each gas is based on the maximum and minimum concentrations of each gas in the training profiles. Hence, predictions cannot be later made for absorber amount values outside that range. Another difficulty with this method is that the input atmospheric profiles of temperature and gas concentrations are expressed on a grid of fixed pressures and must be interpolated to the fixed absorber amounts and the resulting transmittances must be interpolated back to the original pressure grid. Back-and-forth interpolation like this introduces interpolation errors. However, studies suggest that even with this, ODAS results in improved accuracy (Hannon et al., 1996; McMillin et al., 1995a), especially when calculating water vapor Jacobians (Chen et al., 2010).

Regression equations of ODAS have some key differences when compared to ODPS. Because the absorption coefficient is a function of the amount and since ODAS discretizes the atmosphere in terms of integrated path absorber amounts, ODAS regression equations first predict the absorption coefficient which is later converted to optical depth or transmittance values. Another key difference is that ODAS optimally chooses a set of six predictors from a pool of 18 predefined predictors. The functional forms of these predictors are listed in Chen et al. (2010). Unlike ODPS, ODAS uses a polynomial function with integrated gas amount as a dependent variable in the regression equation to estimate the vertical variations of coefficients, instead of deriving separate regression coefficients for each layer. The following regression equation is used by ODAS (Chen et al., 2010):

$$\ln\big(k(A)\big) = c_0(A) + \sum_{j=1}^{6} c_j(A)X_j(A) \tag{2.6}$$

where $k(A)$ is the absorption coefficient for A absorber amount. $c_j(A)$ is given by a polynomial function,

$$c_j(A) = \sum_{m=0}^{n} a_{j,m}A^m, \qquad j = 0, 6;\ n \leq 10 \tag{2.7}$$

where, $a_{j,m}$ are constants obtained through regression. In CRTM, the absorber amount values (A) are brought on the scale of 0 to 1 by the following equation:

$$Z = \frac{1}{\alpha} \ln\left(\frac{A - b_2}{b_1}\right); 0 \leq Z \leq 1, \tag{2.8}$$

where, α is a constant determined by trial and error, and b_1 and b_2 are also constants determined by the minimum and maximum values of A.

2.4 New machine-learning based method

The goal of the new machine-learning based method is to predict layer optical depth as a function of wavelength for a given set of environmental conditions. To train this machine-learning model, values of layer optical depths calculated from MonoRTM were used as the truth, using 8640 atmospheric profiles that covered the diurnal and seasonal range of atmospheric variables, pressure, temperature, and gas concentrations. The method for selecting these 8640 atmospheric profiles is described in detail in Section 2.4.2. Further, the neural network performance is assessed using an independent testing dataset, ECMWF83, which includes 83 profiles for the year 2006–2007 and will be detailed in Section 2.4.3.

2.4.1 Calculating true optical depth values using MonoRTM

MonoRTM is designed to process one or a number of exact monochromatic wavenumbers accurately and efficiently (Clough et al., 2005). Monochromatic Optical Depth Model (MODM) is the core component of MonoRTM handling the calculation of the molecular optical depth. Spectroscopic line parameters inputs from the HITRAN database (Rothman et al., 2013) are included in MonoRTM by running a line file creation program – LNFL. In addition to that, LNFL also includes line coupling parameters and pressure-induced line shifts to the line parameters file used by MonoRTM. Based on this spectroscopic information MonoRTM calculates Voigt line shape functions for all the input atmospheric levels. The Voigt profile, which is a convolution of Lorentz distribution and Gaussian distribution, describes the combined effects of pressure broadening and Doppler broadening (caused due to thermal motion of molecules) on the spectral line shape.

In addition to spectral line parameter information from HITRAN, MonoRTM also incorporates the continuum model MT_CKD (Mlawer et al., 2012). It includes self- and foreign-continuum coefficients for water vapor, carbon dioxide, oxygen, nitrogen, and ozone for the relevant spectral region. The continuum model MT_CKD also includes the temperature dependence of continuum coefficients. All this spectroscopic information including absorption and emission lines as well as the continuum is used by MODM to calculate absorption coefficients and from that, layer optical depths. The atmosphere layering routine LBLATM stratifies the atmosphere in a discrete pressure grid and defines the layer quantities from input profiles on pressure levels. Based on the input pressure and temperature values it also calculates the layer thickness using the hypsometric equation. Additionally, MonoRTM also contains a radiative transfer solver – RTMmono – for calculating radiances.

To train neural networks, the optical depths for 302 exact wavenumbers (see Table 2.1) were calculated from MonoRTM on a fixed pressure grid of 101 pressure levels. MonoRTM was set up for a viewing geometry of a downward-looking sensor at the top-of-atmosphere. The pressure-level grid of 101 levels follows the AIRS science team pressure-level definition (Hannon et al., 1996; Strow et al., 2003). The input atmospheric profiles for the training, validation, and testing datasets will be all based on these 101 levels.

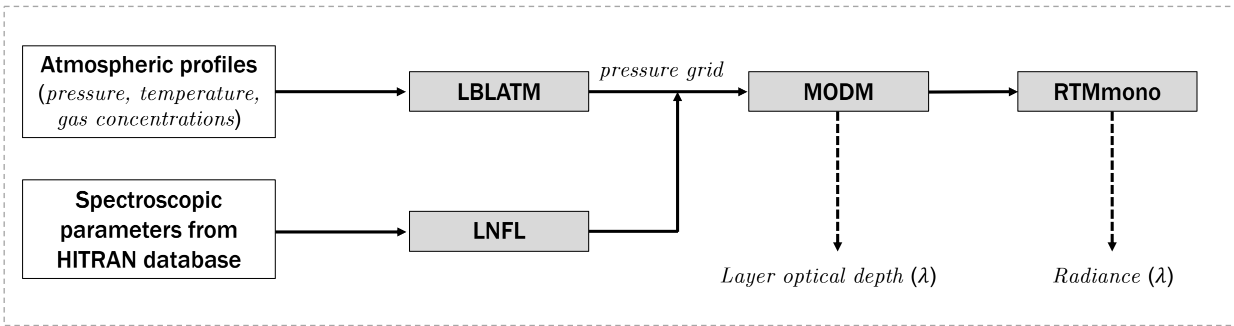

Figure 2.9. Flowchart summarizing the workflow of the line-by-line model, MonoRTM.

2.4.2 Preparation of training and validation dataset

The training and validation datasets are based on 8640 atmospheric profiles selected from ERA5 Reanalysis data from the year 2014. ERA5 is the fifth generation of ECMWF atmospheric reanalysis produced using the 4D-Var data assimilation and model forecasts of the ECMWF Integrated Forecast System (IFS) (Hersbach et al., 2020). It provides hourly estimates for several atmospheric, ocean-wave, and land-surface properties as global gridded data at the horizontal resolution of 0.25 degree.

We chose the year 2014 for our training dataset to avoid large-scale patterns in sea surface temperature (SST) such as those resulting from ENSO. To select a year without ENSO influence, we used two standardized ENSO indices. NOAA Climate Prediction Center and Physical Sciences Laboratory calculates Oceanic Niño Index (ONI) and Multivariate ENSO Index (MEI v2) primarily using SST fields in the ENSO region, along with other variables such as sea level pressure, surface wind, and outgoing longwave radiation. Together these indices provide a gauge of strength on the oceanic and atmospheric part of the ENSO pattern.

The idea of selecting a large set of input atmospheric profiles is to capture the diurnal and seasonal variation of atmospheric state in the training dataset for different climate zones around the world. To ensure such a selection of profiles we sampled data from the 5, 15, and 25th day of each month. For these three days in each month, we randomly select 60 locations around the world and for those locations, we sample data on timesteps 00, 06, 12, and 18 UTC. With this profile selection approach, we generated a dataset of 8640 profiles (3 days x 60 locations x 4 timesteps x 12 months) for 2160 locations (3 days x 60 locations x 12 months) representing diverse environmental conditions. The location of each of these profiles is plotted on a map along with the month and shown in Figure 2.10.

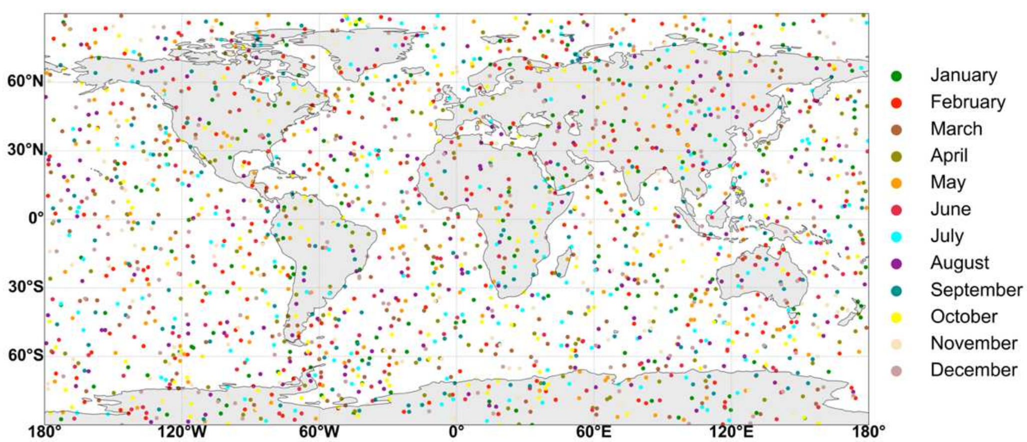

Figure 2.10. Locations of 8640 profiles from ERA5 dataset for the year 2014 with corresponding month.

We use the following variables from the ERA5 Reanalysis dataset: temperature (K), specific humidity (kg/kg), and ozone mass mixing ratio (kg/kg). We use the ERA5 data on 137 hybrid sigma model-levels to sample these variables. The specific humidity is converted to mass mixing ratio (g/kg) for calculating truth and training the neural networks. To keep it consistent with the pressure-level definition described in Section 2.4.1, the profiles are interpolated to 101 levels spanning from 1100 hPa to 0.005 hPa using linear interpolation. Variable at pressure levels having larger pressures than at the surface are set to constant by using the surface values.

As described in Section 2.2.2, there are several CO_2 lines in the center and wings of the channel. To incorporate the effect of present-day CO_2 concentrations on optical depth, we use the Copernicus Atmosphere Monitoring Service's (CAMS) global reanalysis dataset of atmospheric composition (EAC4) for CO_2 profiles. The reanalysis procedure of CAMS combines model data with satellite observations of greenhouse gases into a globally complete and consistent dataset using ECMWF's IFS (Agusti-Panareda et al., 2022). From the CAMS Reanalysis data, we select CO_2 profiles in the Year 2020 (the latest available) for the same location and hour as the ERA5 profiles. The CAMS dataset provides a CO_2 mass mixing ratio (kg/kg) on 25 pressure levels ranging from 1000 hPa to 1 hPa. Similar to the ERA5 dataset, we interpolate CO_2 profiles to 101 pressure levels.

Combined with profiles from the ERA5 dataset and CO_2 profiles from CAMS, we prepare a set of 8640 diverse profiles of temperature, water vapor mixing ratio, carbon dioxide, and ozone for input to MonoRTM for calculating corresponding true layer optical depth values for 302 wavenumbers. After calculating the truth, we split the 8640 profiles into 6912 training profiles (80%) and 1728 validation profiles (20%). As later described in Section 2.4.4, neural networks are trained separately for each of the 302 wavenumbers. This results in 691200 training (6912 profiles x 100 layers) and 172800 (1728 profiles x 100 layers) validation samples for each neural network. The split into training and validation data was carried out ensuring that the diurnal and seasonal variability is still represented in both datasets. The summary of the training and validation data is provided in Table 2.2.

Table 2.2. Minimum and maximum values of input and output values in the training and validation data.

Training Data (ERA5)					
	Temperature (K)	H_2O (g/kg)	CO_2 (ppm)	O_3 (g/kg)	Layer Optical Depth
	Input	*Input*	*Input*	*Input*	*Output*
Maximum value	327.51	22.6	520.4	0.37	3916
Minimum value	162.8	1.8e-05	359.8	4.8e-07	1.69e-13
Validation data (ERA5)					
Maximum value	313.38	21.12	520.4	0.37	3666
Minimum value	163.83	2.8e-06	359.8	7.1e-07	1.79 e-13

2.4.3 Testing dataset

As mentioned in Section 2.4.1, we use a set of 83 diverse profiles on 101 pressure levels from ECMWF, known as ECMWF83 profiles, as the testing dataset for the machine-learning model. The ECMWF83 profiles are commonly used in the remote sensing community to train fast gas absorption parameterization (Chen et al., 2010, 2012; De Angelis et al., 2017; Saunders et al., 2017; Turner et al., 2019). These profiles were sampled for the period July 2006 – June 2007 from a large profile dataset containing 121,462,560 profiles generated using ECMWF's IFS (Chevallier et al., 2006). To ensure that the values of sampled profiles are capturing the range of various environmental parameters, Matricardi (2008) describes the scaling of profiles by using the measurements made by the closest station of NOAA's Climate Monitoring and Diagnostic Laboratory (CMDL) and the Advanced Global Atmospheric Gas Experiment (AGAGE) program. Further, the concentrations for CO_2 profiles were scaled to the year 2009 assuming a rate of increase of 1.85 ppmv/year. In the set of 83 profiles, the last three profiles, i.e., profiles 81 to 83, are respectively the minimum, maximum, and mean of 80 profiles.

From the ECMWF83 profiles, we use the same variables as those from ERA5. True layer optical depths were calculated for the ECMWF83 profiles by running MonoRTM using these variables. The summary of the testing data is provided in Table 2.3.

Table 2.3. Minimum and maximum values of input and output variables in testing data.

Testing Data (ECMWF83)					
	Temperature (K)	H_2O (g/kg)	CO_2 (ppm)	O_3 (g/kg)	Layer Optical Depth
	Input	*Input*	*Input*	*Input*	*Output*
Maximum value	318.26	26.31	399.08	1.78e-02	4826
Minimum value	166.72	9e-06	366.57	1.15e-05	1.13e-13

2.4.4 Neural network emulator for predicting layer optical depths

Section 2.2.2 describes the characteristics of gas absorption in the spectral interval of the new water vapor channel centered at wavelength 5.15 µm. The section also describes the complex structure of the absorption spectrum in the channel marked by sharp changes in absorption coefficients as shown in Figure 2.5. To ensure the best possible spectral performance of the neural network, we trained each wavelength in the spectral interval of the channel individually. The goal of the neural network is to predict layer optical depths as a function of wavelength for a given atmospheric input profile. As explained in Section 2.1, the optical depth value changes with temperature, pressure, and gas concentration – and thus they constitute crucial predictors of the layer optical depth. Since we calculate true optical depth values on a fixed pressure grid of 100 layers, input pressure rather works as a coordinate than a variable.

The neural networks used for training all the wavelengths have 6 layers (*1 input* + *5 hidden*) and 100 nodes. Layer values of pressure, temperature, water vapor, carbon dioxide, and ozone are inputs, and layer optical depths on 100 layers are outputs of the neural network. For all the neural networks, the input values are the same but the output layer optical depth changes as a function of wavelength. All input variables except temperature vary on several orders of magnitude and therefore are log-scaled before training. They are further standardized by subtracting the mean and dividing by the standard deviation before training. Additionally, all the layers and nodes in the networks are trained with the activation function – Rectified Linear Unit (ReLU) (Agarap, 2019). The training was carried out in a feed-forward manner by optimizing the gradient calculations with Adam optimizer (Kingma & Ba, 2017) and using mean squared error (MSE) as a loss function between the predicted and true values. The flowchart shown in Figure 2.11 illustrates the neural network set-up used in the study.

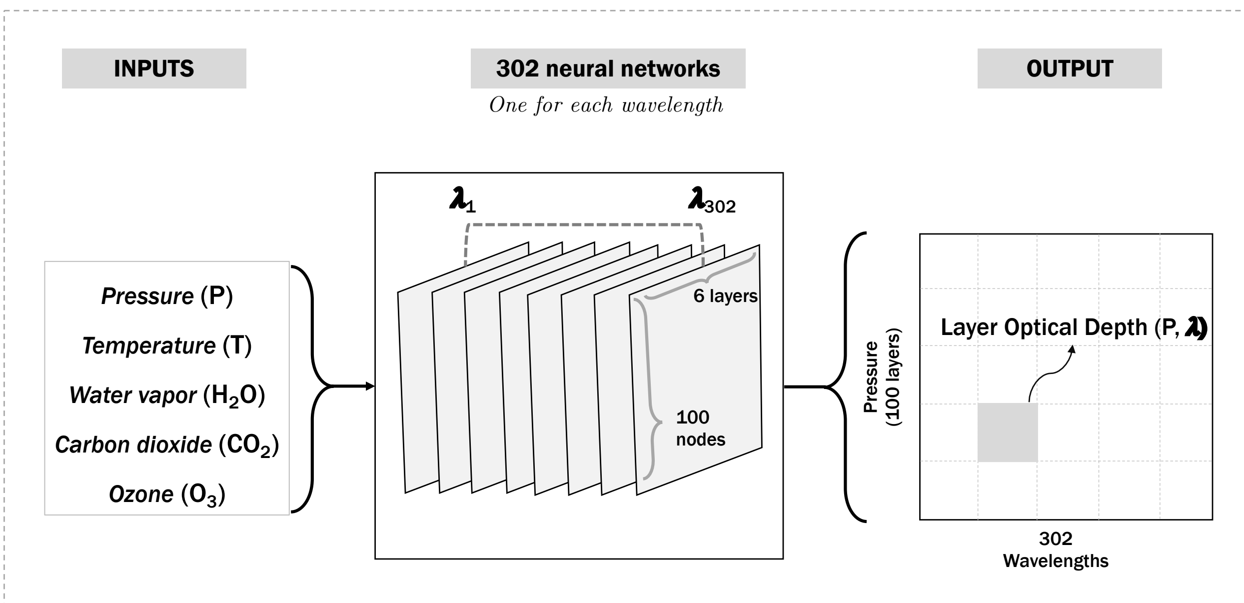

Figure 2.11. Schematic illustrating the neural network architecture of the neural networks used in this study.

The neural networks are trained to predict monochromatic layer optical depth values as a function of wavelength. The spectral layer optical depth values can be later convolved with the spectral response function of a given channel to calculate the channel-specific values, which can be further converted to layer-to-space transmittance values that are used as input by the radiative transfer equation of CRTM. Since these steps are purely arithmetic in nature, it has no additional computational burden.

3.1 Predictions using machine-learning methods

As discussed in Section 2.4.2, the neural networks emulating layer optical depths as a function of wavelength are trained using atmospheric profiles from the ERA5 reanalysis dataset for the year 2014 as training and validation data, and the performance is evaluated against ECMWF83 profiles that correspond to the period 2006-2007. Further, with a goal to incorporate the latest available carbon dioxide concentrations we used CO_2 profiles from CAMS global atmospheric composition reanalysis data for the year 2020. This resulted in a completely different distribution of carbon dioxide concentration values between training and testing data as shown in Figure 3.1 (a). To be able to evaluate the performance of wavelengths that are absorbed by CO_2, the CAMS profiles for 2020 are scaled with a random values value between 0.9 and 1.1. As a result, the CO_2 concentrations used in the training and validation data encompass testing data values and future concentrations. The histogram of scaled values is shown in Figure 3.1 (b).

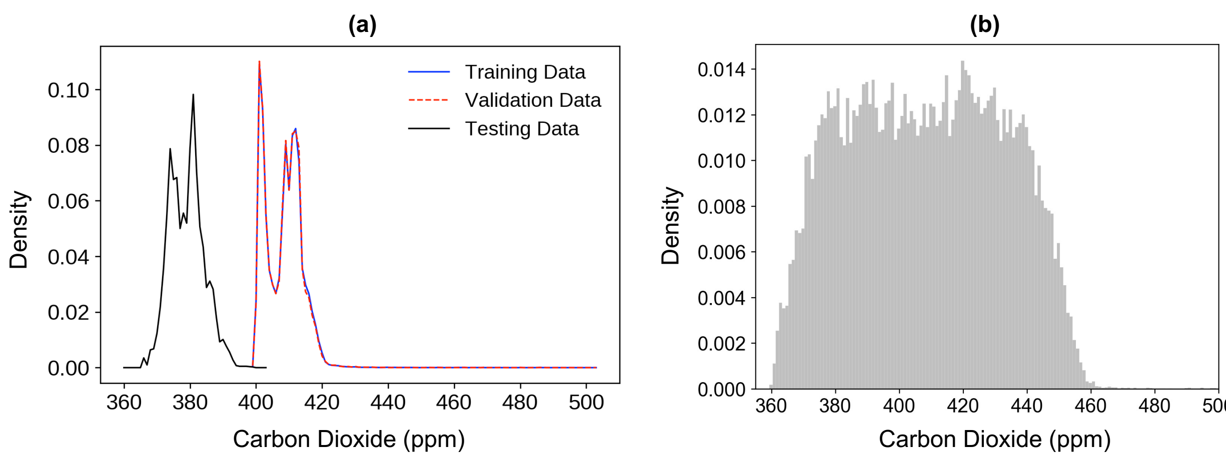

Figure 3.1. (a) Histogram of original training and validation data from CAMS reanalysis for the year 2020, respectively in blue solid line and red dashed line, with testing data from ECMWF83 profiles for the year 2006-2007 shown with the solid green line. (b) Histogram of scaled training and validation data.

3.1.1 Performance of neural network predictions

The line-by-line predictions of layer optical depth values for ECMWF83 profiles are compared with true values calculated using MonoRTM. The comparison of NN predicted values with true values is shown with a density scatter plot in Figure 3.2 (a). The scatter plot demonstrates the accurate prediction of optical depth values with points having the highest density closely following the one-to-one line. The layer optical depth values vary over several orders of magnitude with the lowest optical depth values generally occurring in the upper part of the atmosphere and in the weakly absorbing wavelengths. Further, there is large variability in optical depth values with wavelength due to the absorption coefficient spectrum showing sharp changes in this spectral interval as shown in Figure 2.5. Therefore, in order to compare the performance for wavelengths having different absorbing strengths we calculate the percent error between predicted and true optical depth values for 100 layers and 302 wavelengths of 83 testing data profiles. The error histogram of predicted optical depths is shown in Figure 3.2 (b). The mean percent error of neural network predictions of line-by-line layer optical depths for testing data is 0.47%.

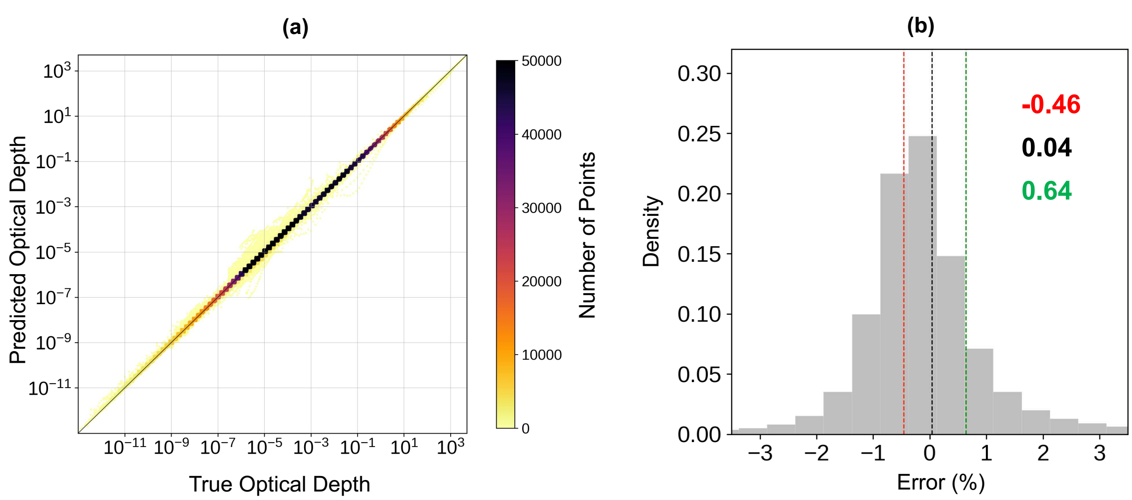

Figure 3.2. (a) Density scatter plot comparing predicted line-by-line layer optical depth values with truth calculated using MonoRTM. The black solid line represents the one-to-one line. (b) Corresponding error histogram with percent error on the x-axis and the corresponding density on the y-axis. The red, black, and green vertical dashed lines represent the 25th, 50th, and 75th percentiles of the predicted percent error with their values noted in matching colors.

3.2 Performance on channel quantities

3.2.1 Transmittance profiles

The radiative transfer code of CRTM requires channel transmittance profiles as input for radiative transfer calculations. To evaluate the performance of neural networks on channel transmittances, the predicted and true line-by-line layer optical depths values are convolved with SRF to calculate the channel layer-to-space transmittance profiles. The scatter plot comparing predicted transmittance values for all 83 profiles with true values is shown in Figure 3.3 (a). The corresponding error histogram is shown in Figure 3.3 (b). The scatter plot shows that accurate channel transmittance can be calculated using the line-by-line values predicted using the neural networks. Since channel transmittance values are convolved over SRF, it is not a function of wavelength and as shown in the histogram (Figure 3.3b), the error metric significantly improves. The mean percent error of transmittance values calculated using predicted line-by-line values is 0.02%. The ECMWF83 profile set provides minimum, maximum, and mean profiles. The transmittance profiles calculated using predicted and true values for maximum and mean profiles are shown in Figure 3.3 (c and d).

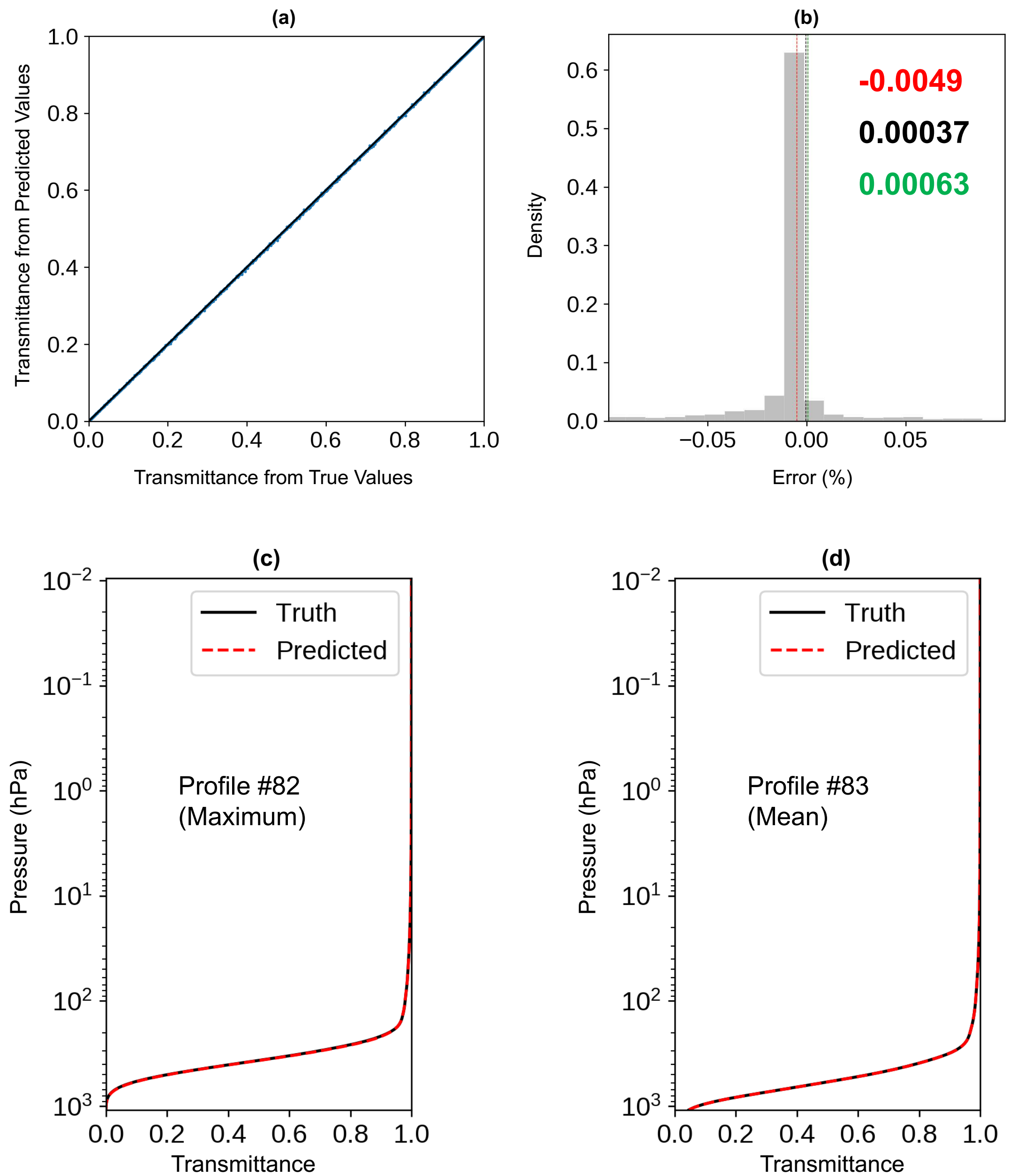

Figure 3.3. (a) Scatter plot comparing layer-to-space channel transmittance values calculated using predicted and true line-by-line values. (b) Corresponding error histogram showing the percent error density of predicted values. The red, black, and green vertical dashed lines represent the 25th, 50th, and 75th percentiles of the predicted percent error with their values noted in matching colors. (c and d) Comparison of layer-to-space channel transmittance profiles calculated using predicted and true values of maximum and mean profiles of ECMWF83 dataset.

3.2.2 *Weighting functions*

Weighting functions are important indicators of the accuracy with which predicted transmittance values are sensitive to the correct atmospheric layer. To build confidence in using the neural networks for calculating weighting functions of future hypothetical sensors, weighting functions are calculated for all 83 test profiles using the predicted and true line-by-line layer optical depth values and the sensor response function of the channel. The weighting function values calculated using predicted and true values are compared in a scatter plot in Figure 3.4 (a). It demonstrates the accuracy of predicted line-by-line values in calculating channel weighting functions. The corresponding error histogram is shown in Figure 3.4(b). Similarly, as transmittance profiles in Section 3.2.1, the weighting functions calculated using predicted and true values for maximum and mean profiles are shown respectively in Figure 3.4 (c and d).

3.3 Summary of error statistics

The error statistics of neural network predictions are summarized in Table 3.1.

Table 3.1. Error statistics of the performance of emulators on optical depths at 302 wavelengths, and profiles of layer-to-top channel transmittance and weighting function using the testing dataset. Mean, 25th, 50th, and 75th percentile errors are listed in %.

Predicted variable	25th (%)	50th (%)	75th (%)	Mean (%)
Optical depth	–0.46	0.04	0.64	0.47
Layer-to-top channel transmittance	–0.0049	0.00037	0.00063	0.02
Channel weighting functions	–0.31	0.021	0.4	0.13

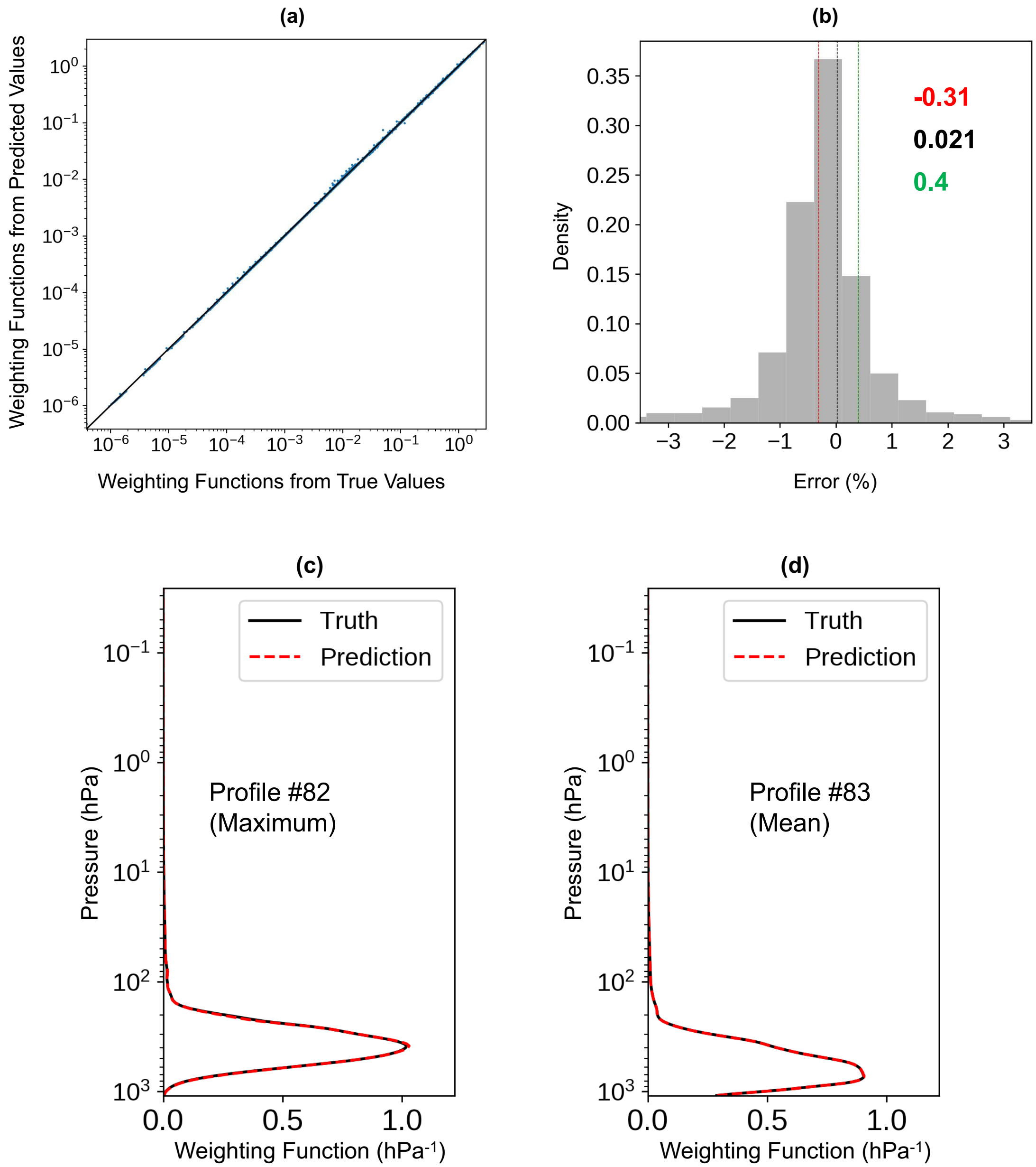

Figure 3.4. Same as Figure 3.3, but for weight functions.

CHAPTER 4: SUMMARY AND CONCLUSIONS

4.1 Summary and key results

Significant progress has been made over the past decades to expand the environmental parameters being monitored from satellite platforms. This has added immense value to our modeling and forecasting efforts through improved data assimilation. Accurate and efficient methods of performing gas absorption calculations in the forward radiative transfer models are critical for satellite retrievals, radiance simulation, and future satellite mission designs. In most radiative transfer models such as CRTM, gas absorptions are parameterized using conventional regression methods and the regression coefficients are saved specifically for known sensors. This greatly restricts the effort of designing new channels for future hypothetical sensors. Simulating satellite radiances using CRTM for these new sensors requires the ability to efficiently and accurately calculate line-by-line values for any given spectral interval.

In this thesis, we demonstrated a method of training neural networks that predicts line-by-line layer optical depths using an example spectral interval of a new infrared water vapor channel on an upcoming GeoXO mission. This spectral interval includes 302 spectral points at a very fine spectral resolution of 0.0014 μm and is largely absorbed by three gases, water vapor, carbon dioxide, and ozone. With a large variability in optical depth values with wavelength due to sharp changes in absorption coefficients at this spectral resolution and changes in the dominant absorber with pressure, the spectral interval used here is a representative example of the infrared spectral region.

The performance of trained neural networks was evaluated against the completely independent ECMWF83 profiles as testing data. These are 83 profiles carefully sampled by ECMWF from a large dataset of about 121 million profiles representing a wide range of atmospheric variables. We showed that the neural networks are accurately able to predict the line-by-line layer optical depth values with a mean percent error of 0.47%. This demonstrates the feasibility of using neural networks in computing line-by-line values.

To simulate the channel radiances observed by a satellite instrument, CRTM requires profiles of channel layer-to-space transmittances. These profiles were calculated using the predicted line-by-line layer optical depth values from neural networks. We showed that the transmittance values calculated from predicted values are accurate with a mean percent error of 0.02%. This illustrates that the predicted line-by-line values can be later convolved with a given sensor response function to facilitate the radiance simulations using CRTM.

An important aspect of designing hypothetical channels for a new sensor is the ability to accurately calculate channel weighting functions. To build confidence in using the neural network calculations for this purpose, the channel weighting functions were calculated for predicted and true line-by-line values. We showed that the predicted values accurately calculate channel weighting functions with a mean percent error of 0.13%.

4.2 Conclusions

The method presented in the thesis demonstrates the feasibility of using neural networks for accurately predicting line-by-line layer optical depths. For a given sensor response function, the line-by-line values can be easily converted to channel transmittance values later. As a result, the method presented here can also be used operationally.

The goal of the present study is to close the important gap in the ability to facilitate CRTM simulations for a given spectral interval of new channels which was previously not possible with ODAS and ODPS. The method developed in this thesis achieves the goal by demonstrating accurate predictions of line-by-line layer optical depths. With the accurate calculations of channel transmittance profiles and channel weighting functions, the feasibility of using neural networks for designing new channels is demonstrated.

4.3 Future work

We have shown the feasibility of using machine-learning methods to emulate line-by-line layer optical depths with a limited example of a channel in thermal infrared. The simple structure of this method makes it flexible enough to expand it to other spectral intervals and regions in the electromagnetic spectrum such as microwave. This can be easily carried out by incorporating the layer concentration values of relevant absorbing constituents for the spectral region of interest. Similarly, the method can be easily extended to the whole infrared or microwave spectral region. This can result in a powerful tool that outputs line-by-line values for any arbitrary spectral interval, that can be convolved with a given sensor response function to calculate channel quantities.

While the performance evaluation against the testing dataset shows a mean error of 0.02% only in the layer-to-space atmospheric transmittance, it is important to compare the performance of the emulator to that of the simple regression model currently used in CRTM, which will be part of future work.

Another important component of future work is the integration of neural network predictions into the CRTM workflow. This integration can be tested with existing ODAS and ODPS to compare the impact of these methods on simulated satellite radiances in terms of accuracy and speed.

REFERENCES

Adkins, J., Alsheimer, F., Ardanuy, P., Boukabara, S., Casey, S., Coakley, M., Conran, J., Cucurull, L., Daniels, J., Ditchek, S. D., Gallagher, F., Garrett, K., Gerth, J., Goldberg, M., Goodman, S., Grigsby, E., Griffin, M., Griffin, V., Hardesty, M., … Yoe, J. (2021). *Geostationary Extended Observations (GeoXO) Hyperspectral InfraRed Sounder Value Assessment Report* (noaa:32921). https://doi.org/10.25923/7zvz-fv26

Agarap, A. F. (2019). *Deep Learning using Rectified Linear Units (ReLU)* (arXiv:1803.08375). arXiv. https://doi.org/10.48550/arXiv.1803.08375

Agusti-Panareda, A., Barré, J., Massart, S., Inness, A., Aben, I., Ades, M., Baier, B. C., Balsamo, G., Borsdorff, T., Bousserez, N., Boussetta, S., Buchwitz, M., Cantarello, L., Crevoisier, C., Engelen, R., Eskes, H., Flemming, J., Garrigues, S., Hasekamp, O., … Wu, L. (2022). Technical note: The CAMS greenhouse gas reanalysis from 2003 to 2020. *EGUsphere*, 1–51. https://doi.org/10.5194/egusphere-2022-283

Allan, R. P. (2012). The Role of Water Vapour in Earth’s Energy Flows. *Surveys in Geophysics*, *33*(3), 557–564. https://doi.org/10.1007/s10712-011-9157-8

Allan, R. P., Shine, K. P., Slingo, A., & Pamment, J. A. (1999). The dependence of clear-sky outgoing long-wave radiation on surface temperature and relative humidity. *Quarterly Journal of the Royal Meteorological Society*, *125*(558), 2103–2126. https://doi.org/10.1002/qj.49712555809

Bauer, P., Thorpe, A., & Brunet, G. (2015). The quiet revolution of numerical weather prediction. *Nature*, *525*(7567), Article 7567. https://doi.org/10.1038/nature14956

Blackwell, W. J., Bickmeier, L. J., Leslie, R. V., Pieper, M. L., Samra, J. E., Surussavadee, C., & Upham, C. A. (2011). Hyperspectral Microwave Atmospheric Sounding. *IEEE*

Transactions on Geoscience and Remote Sensing, *49*(1), 128–142. https://doi.org/10.1109/TGRS.2010.2052260

Boukabara, S.-A., Krasnopolsky, V., Stewart, J. Q., Maddy, E. S., Shahroudi, N., & Hoffman, R. N. (2019). Leveraging Modern Artificial Intelligence for Remote Sensing and NWP: Benefits and Challenges. *Bulletin of the American Meteorological Society*, *100*(12), ES473–ES491. https://doi.org/10.1175/BAMS-D-18-0324.1

Brenowitz, N. D., & Bretherton, C. S. (2018). Prognostic Validation of a Neural Network Unified Physics Parameterization. *Geophysical Research Letters*, *45*(12), 6289–6298. https://doi.org/10.1029/2018GL078510

Bretherton, C. S., Peters, M. E., & Back, L. E. (2004). Relationships between Water Vapor Path and Precipitation over the Tropical Oceans. *Journal of Climate*, *17*(7), 1517–1528. https://doi.org/10.1175/1520-0442(2004)017<1517:RBWVPA>2.0.CO;2

Buehler, S. A., Eriksson, P., & Lemke, O. (2011). Absorption lookup tables in the radiative transfer model ARTS. *Journal of Quantitative Spectroscopy and Radiative Transfer*, *112*(10), 1559–1567. https://doi.org/10.1016/j.jqsrt.2011.03.008

Capelle, V., Chédin, A., Péquignot, E., Schlüssel, P., Newman, S. M., & Scott, N. A. (2012). Infrared Continental Surface Emissivity Spectra and Skin Temperature Retrieved from IASI Observations over the Tropics. *Journal of Applied Meteorology and Climatology*, *51*(6), 1164–1179. https://doi.org/10.1175/JAMC-D-11-0145.1

Chen, Y., Han, Y., Van Delst, P., & Weng, F. (2010). On water vapor Jacobian in fast radiative transfer model. *Journal of Geophysical Research: Atmospheres*, *115*(D12). https://doi.org/10.1029/2009JD013379

Chen, Y., Han, Y., & Weng, F. (2012). Comparison of two transmittance algorithms in the community radiative transfer model: Application to AVHRR. *Journal of Geophysical Research: Atmospheres*, *117*(D6). https://doi.org/10.1029/2011JD016656

Chevallier, F., Chéruy, F., Scott, N. A., & Chédin, A. (1998). A Neural Network Approach for a Fast and Accurate Computation of a Longwave Radiative Budget. *Journal of Applied Meteorology and Climatology*, *37*(11), 1385–1397. https://doi.org/10.1175/1520-0450(1998)037<1385:ANNAFA>2.0.CO;2

Chevallier, F., Michele, S. D., & McNally, A. P. (2006). *Diverse profile datasets from the ECMWF 91-level short-range forecasts*.

Chevallier, F., Morcrette, J.-J., Chéruy, F., & Scott, N. A. (2000). Use of a neural-network-based long-wave radiative-transfer scheme in the ECMWF atmospheric model. *Quarterly Journal of the Royal Meteorological Society*, *126*(563), 761–776. https://doi.org/10.1002/qj.49712656318

Clough, S. A., Shephard, M. W., Mlawer, E. J., Delamere, J. S., Iacono, M. J., Cady-Pereira, K., Boukabara, S., & Brown, P. D. (2005). Atmospheric radiative transfer modeling: A summary of the AER codes. *Journal of Quantitative Spectroscopy and Radiative Transfer*, *91*(2), 233–244. https://doi.org/10.1016/j.jqsrt.2004.05.058

Crevoisier, C., Clerbaux, C., Guidard, V., Phulpin, T., Armante, R., Barret, B., Camy-Peyret, C., Chaboureau, J.-P., Coheur, P.-F., Crépeau, L., Dufour, G., Labonnote, L., Lavanant, L., Hadji-Lazaro, J., Herbin, H., Jacquinet-Husson, N., Payan, S., Péquignot, E., Pierangelo, C., … Stubenrauch, C. (2014). Towards IASI-New Generation (IASI-NG): Impact of improved spectral resolution and radiometric noise on the retrieval of thermodynamic, chemistry and climate variables. *Atmospheric Measurement Techniques*, *7*(12), 4367–4385. https://doi.org/10.5194/amt-7-4367-2014

De Angelis, F., Cimini, D., Löhnert, U., Caumont, O., Haefele, A., Pospichal, B., Martinet, P., Navas-Guzmán, F., Klein-Baltink, H., Dupont, J.-C., & Hocking, J. (2017). Long-term observations minus background monitoring of ground-based brightness temperatures from a microwave radiometer network. *Atmospheric Measurement Techniques*, *10*(10), 3947–3961. https://doi.org/10.5194/amt-10-3947-2017

de F. Forster, P. M., & Shine, K. P. (1999). Stratospheric water vapour changes as a possible contributor to observed stratospheric cooling. *Geophysical Research Letters*, *26*(21), 3309–3312. https://doi.org/10.1029/1999GL010487

de Vries, A. J. (2021). A global climatological perspective on the importance of Rossby wave breaking and intense moisture transport for extreme precipitation events. *Weather and Climate Dynamics*, *2*(1), 129–161. https://doi.org/10.5194/wcd-2-129-2021

Dessler, A. E., Schoeberl, M. R., Wang, T., Davis, S. M., & Rosenlof, K. H. (2013). Stratospheric water vapor feedback. *Proceedings of the National Academy of Sciences*, *110*(45), 18087–18091. https://doi.org/10.1073/pnas.1310344110

Di, D., Li, J., Li, Z., Li, J., Schmit, T. J., & Menzel, W. P. (2021). Can Current Hyperspectral Infrared Sounders Capture the Small Scale Atmospheric Water Vapor Spatial Variations? *Geophysical Research Letters*, *48*(21), e2021GL095825. https://doi.org/10.1029/2021GL095825

Eyre, J. R. (1991). *A fast radiative transfer model for satellite sounding systems* [Text]. ECMWF. https://www.ecmwf.int/en/elibrary/74431-fast-radiative-transfer-model-satellite-sounding-systems

Eyre, J. R., & Woolf, H. M. (1988). Transmittance of atmospheric gases in the microwave region: A fast model. *Applied Optics*, *27*(15), 3244–3249. https://doi.org/10.1364/AO.27.003244

Fasullo, J. T., & Trenberth, K. E. (2008). The Annual Cycle of the Energy Budget. Part I: Global Mean and Land–Ocean Exchanges. *Journal of Climate*, *21*(10), 2297–2312. https://doi.org/10.1175/2007JCLI1935.1

Fleming, H. E., & McMillin, L. M. (1977). Atmospheric transmittance of an absorbing gas. 2: A computationally fast and accurate transmittance model for slant paths at different zenith angles. *Applied Optics*, *16*(5), 1366–1370. https://doi.org/10.1364/AO.16.001366

Forster, P. M. de F., & Shine, K. P. (2002). Assessing the climate impact of trends in stratospheric water vapor. *Geophysical Research Letters*, *29*(6), 10-1-10–14. https://doi.org/10.1029/2001GL013909

Goldberg, M. D., & Weng, F. (2006). Advanced Technology Microwave Sounder. In J. J. Qu, W. Gao, M. Kafatos, R. E. Murphy, & V. V. Salomonson (Eds.), *Earth Science Satellite Remote Sensing: Vol. 1: Science and Instruments* (pp. 243–253). Springer. https://doi.org/10.1007/978-3-540-37293-6_13

Hannon, S. E., Strow, L. L., & McMillan, W. W. (1996). Atmospheric infrared fast transmittance models: A comparison of two approaches. *Optical Spectroscopic Techniques and Instrumentation for Atmospheric and Space Research II*, *2830*, 94–105. https://doi.org/10.1117/12.256106

Held, I. M., & Soden, B. J. (2000). Water Vapor Feedback and Global Warming. *Annual Review of Energy and the Environment*, *25*(1), 441–475. https://doi.org/10.1146/annurev.energy.25.1.441

Hersbach, H., Bell, B., Berrisford, P., Hirahara, S., Horányi, A., Muñoz-Sabater, J., Nicolas, J., Peubey, C., Radu, R., Schepers, D., Simmons, A., Soci, C., Abdalla, S., Abellan, X., Balsamo, G., Bechtold, P., Biavati, G., Bidlot, J., Bonavita, M., … Thépaut, J.-N. (2020). The ERA5 global reanalysis. *Quarterly Journal of the Royal Meteorological Society*, *146*(730), 1999–2049. https://doi.org/10.1002/qj.3803

Hocking, J., Vidot, J., Brunel, P., Roquet, P., Silveira, B., Turner, E., & Lupu, C. (2021). A new gas absorption optical depth parameterisation for RTTOV version 13. *Geoscientific Model Development*, *14*(5), 2899–2915. https://doi.org/10.5194/gmd-14-2899-2021

Holmlund, K., Grandell, J., Schmetz, J., Stuhlmann, R., Bojkov, B., Munro, R., Lekouara, M., Coppens, D., Viticchie, B., August, T., Theodore, B., Watts, P., Dobber, M., Fowler, G., Bojinski, S., Schmid, A., Salonen, K., Tjemkes, S., Aminou, D., & Blythe, P. (2021). Meteosat Third Generation (MTG): Continuation and Innovation of Observations from Geostationary Orbit. *Bulletin of the American Meteorological Society*, *102*(5), E990–E1015. https://doi.org/10.1175/BAMS-D-19-0304.1

Isaacs, R. G., Hoffman, R. N., & Kaplan, L. D. (1986). Satellite remote sensing of meteorological parameters for global numerical weather prediction. *Reviews of Geophysics*, *24*(4), 701–743. https://doi.org/10.1029/RG024i004p00701

Joo, S., Eyre, J., & Marriott, R. (2013). The Impact of MetOp and Other Satellite Data within the Met Office Global NWP System Using an Adjoint-Based Sensitivity Method. *Monthly Weather Review*, *141*(10), 3331–3342. https://doi.org/10.1175/MWR-D-12-00232.1

Kiehl, J. T., & Trenberth, K. E. (1997). Earth's Annual Global Mean Energy Budget. *Bulletin of the American Meteorological Society*, *78*(2), 197–208. https://doi.org/10.1175/1520-0477(1997)078<0197:EAGMEB>2.0.CO;2

Kim, H., Pendergrass, A. G., & Kang, S. M. (2022). The Dependence of Mean Climate State on Shortwave Absorption by Water Vapor. *Journal of Climate*, *35*(7), 2189–2207. https://doi.org/10.1175/JCLI-D-21-0417.1

King, M. D. (1992, January 1). *Remote sensing of cloud, aerosol and water vapor properties from the Moderate Resolution Imaging Spectrometer (MODIS)*. https://ntrs.nasa.gov/citations/19950057640

King, M. D., Menzel, W. P., Kaufman, Y. J., Tanre, D., Gao, B.-C., Platnick, S., Ackerman, S. A., Remer, L. A., Pincus, R., & Hubanks, P. A. (2003). Cloud and aerosol properties, precipitable water, and profiles of temperature and water vapor from MODIS. *IEEE Transactions on Geoscience and Remote Sensing*, *41*(2), 442–458. https://doi.org/10.1109/TGRS.2002.808226

Kingma, D. P., & Ba, J. (2017). *Adam: A Method for Stochastic Optimization* (arXiv:1412.6980). arXiv. https://doi.org/10.48550/arXiv.1412.6980

Kochanov, R. V., Gordon, I. E., Rothman, L. S., Wcisło, P., Hill, C., & Wilzewski, J. S. (2016). HITRAN Application Programming Interface (HAPI): A comprehensive approach to working with spectroscopic data. *Journal of Quantitative Spectroscopy and Radiative Transfer*, *177*, 15–30. https://doi.org/10.1016/j.jqsrt.2016.03.005

Krasnopolsky, V. M., Fox-Rabinovitz, M. S., & Belochitski, A. A. (2008). Decadal Climate Simulations Using Accurate and Fast Neural Network Emulation of Full, Longwave and Shortwave, Radiation. *Monthly Weather Review*, *136*(10), 3683–3695. https://doi.org/10.1175/2008MWR2385.1

Li, J., Liu, C.-Y., Zhang, P., & Schmit, T. J. (2012). Applications of Full Spatial Resolution Space-Based Advanced Infrared Soundings in the Preconvection Environment. *Weather and Forecasting*, *27*(2), 515–524. https://doi.org/10.1175/WAF-D-10-05057.1

Liu, Q., van Delst, P., Chen, Y., Groff, D., Han, Y., Collard, A., Weng, F., Boukabara, S.-A., & Derber, J. (2012). Community radiative transfer model for radiance assimilation and applications. *2012 IEEE International Geoscience and Remote Sensing Symposium*, 3700–3703. https://doi.org/10.1109/IGARSS.2012.6350612

Liu, X., Sr, W. L. S., Zhou, D. K., & Larar, A. M. (2005). A principal component-based radiative transfer forward model (PCRTM) for hyperspectral instruments. *Multispectral and Hyperspectral Remote Sensing Instruments and Applications II*, *5655*, 96–105. https://doi.org/10.1117/12.578996

Löhnert, U., Turner, D. D., & Crewell, S. (2009). Ground-Based Temperature and Humidity Profiling Using Spectral Infrared and Microwave Observations. Part I: Simulated Retrieval Performance in Clear-Sky Conditions. *Journal of Applied Meteorology and Climatology*, *48*(5), 1017–1032. https://doi.org/10.1175/2008JAMC2060.1

Matricardi, M. (2008). *The generation of RTTOV regression coefficients for IASI and AIRS using a new profile training set and a new line-by-line database.* https://www.ecmwf.int/en/elibrary/75607-generation-rttov-regression-coefficients-iasi-and-airs-using-new-profile-training

Matricardi, M., Chevallier, F., Kelly, G., & Thépaut, J.-N. (2004). An improved general fast radiative transfer model for the assimilation of radiance observations. *Quarterly Journal of the Royal Meteorological Society*, *130*(596), 153–173. https://doi.org/10.1256/qj.02.181

McMillin, L. M., Crone, L. J., Goldberg, M. D., & Kleespies, T. J. (1995a). Atmospheric transmittance of an absorbing gas. 4. OPTRAN: A computationally fast and accurate transmittance model for absorbing gases with fixed and with variable mixing ratios at variable viewing angles. *Applied Optics*, *34*(27), 6269–6274. https://doi.org/10.1364/AO.34.006269

McMillin, L. M., Crone, L. J., & Kleespies, T. J. (1995b). Atmospheric transmittance of an absorbing gas. 5. Improvements to the OPTRAN approach. *Applied Optics*, *34*(36), 8396–8399. https://doi.org/10.1364/AO.34.008396

McMillin, L. M., & Fleming, H. E. (1976). Atmospheric transmittance of an absorbing gas: A computationally fast and accurate transmittance model for absorbing gases with constant mixing ratios in inhomogeneous atmospheres. *Applied Optics*, *15*(2), 358–363. https://doi.org/10.1364/AO.15.000358

McMillin, L. M., Fleming, H. E., & Hill, M. L. (1979). Atmospheric transmittance of an absorbing gas. 3: A computationally fast and accurate transmittance model for absorbing gases with variable mixing ratios. *Applied Optics*, *18*(10), 1600–1606. https://doi.org/10.1364/AO.18.001600

McMillin, L. M., Xiong, X., Han, Y., Kleespies, T. J., & Delst, P. V. (2006). Atmospheric transmittance of an absorbing gas. 7. Further improvements to the OPTRAN 6 approach. *Applied Optics*, *45*(9), 2028–2034. https://doi.org/10.1364/AO.45.002028

Menzel, W. P., Schmit, T. J., Zhang, P., & Li, J. (2018). Satellite-Based Atmospheric Infrared Sounder Development and Applications. *Bulletin of the American Meteorological Society*, *99*(3), 583–603. https://doi.org/10.1175/BAMS-D-16-0293.1

Mlawer, E. J., Payne, V. H., Moncet, J.-L., Delamere, J. S., Alvarado, M. J., & Tobin, D. C. (2012). Development and recent evaluation of the MT_CKD model of continuum absorption. *Philosophical Transactions of the Royal Society A: Mathematical, Physical and Engineering Sciences*, *370*(1968), 2520–2556. https://doi.org/10.1098/rsta.2011.0295

Mlawer, E. J., Taubman, S. J., Brown, P. D., Iacono, M. J., & Clough, S. A. (1997). Radiative transfer for inhomogeneous atmospheres: RRTM, a validated correlated-k model for the longwave. *Journal of Geophysical Research: Atmospheres*, *102*(D14), 16663–16682. https://doi.org/10.1029/97JD00237

Moncet, J.-L., Uymin, G., & Snell, H. E. (2004). Atmospheric radiance modeling using the optimal spectral sampling (OSS) method. *Algorithms and Technologies for Multispectral, Hyperspectral, and Ultraspectral Imagery X*, *5425*, 368–374. https://doi.org/10.1117/12.541006

O'Gorman, P. A., & Dwyer, J. G. (2018). Using Machine Learning to Parameterize Moist Convection: Potential for Modeling of Climate, Climate Change, and Extreme Events. *Journal of Advances in Modeling Earth Systems*, *10*(10), 2548–2563. https://doi.org/10.1029/2018MS001351

Rasp, S., & Lerch, S. (2018). Neural Networks for Postprocessing Ensemble Weather Forecasts. *Monthly Weather Review*, *146*(11), 3885–3900. https://doi.org/10.1175/MWR-D-18-0187.1

Rasp, S., Pritchard, M. S., & Gentine, P. (2018). Deep learning to represent subgrid processes in climate models. *Proceedings of the National Academy of Sciences*, *115*(39), 9684–9689. https://doi.org/10.1073/pnas.1810286115

Rothman, L. S., Gordon, I. E., Babikov, Y., Barbe, A., Chris Benner, D., Bernath, P. F., Birk, M., Bizzocchi, L., Boudon, V., Brown, L. R., Campargue, A., Chance, K., Cohen, E. A., Coudert, L. H., Devi, V. M., Drouin, B. J., Fayt, A., Flaud, J.-M., Gamache, R. R., … Wagner, G. (2013). The HITRAN2012 molecular spectroscopic database. *Journal of Quantitative Spectroscopy and Radiative Transfer*, *130*, 4–50. https://doi.org/10.1016/j.jqsrt.2013.07.002

Rutz, J. J., Shields, C. A., Lora, J. M., Payne, A. E., Guan, B., Ullrich, P., O'Brien, T., Leung, L. R., Ralph, F. M., Wehner, M., Brands, S., Collow, A., Goldenson, N., Gorodetskaya, I., Griffith, H., Kashinath, K., Kawzenuk, B., Krishnan, H., Kurlin, V., … Viale, M. (2019). The Atmospheric River Tracking Method Intercomparison Project (ARTMIP): Quantifying Uncertainties in Atmospheric River Climatology. *Journal of Geophysical Research: Atmospheres*, *124*(24), 13777–13802. https://doi.org/10.1029/2019JD030936

Saunders, R., Brunel, P., English, S., Bauer, P., O'Keeffe, U., Francis, P., & Rayer, P. (2006). *RTTOV-8—SCIENCE AND VALIDATION REPORT*.

Saunders, R., Hocking, J., Rundle, D., Rayer, P., Havemann, S., Matricardi, M., Geer, A., Lupu, C., Brunel, P., & Vidot, J. (2017). *RTTOV-12 SCIENCE AND VALIDATION REPORT*.

Saunders, R., Matricardi, M., & Brunel, P. (1999). An improved fast radiative transfer model for assimilation of satellite radiance observations. *Quarterly Journal of the Royal Meteorological Society*, *125*(556), 1407–1425. https://doi.org/10.1002/qj.1999.49712555615

Saunders, R., Rayer, P., Brunel, P., von Engeln, A., Bormann, N., Strow, L., Hannon, S., Heilliette, S., Liu, X., Miskolczi, F., Han, Y., Masiello, G., Moncet, J.-L., Uymin, G., Sherlock, V., & Turner, D. S. (2007). A comparison of radiative transfer models for simulating Atmospheric Infrared Sounder (AIRS) radiances. *Journal of Geophysical Research: Atmospheres*, *112*(D1). https://doi.org/10.1029/2006JD007088

Schmit, T. J., Li, J., Ackerman, S. A., & Gurka, J. J. (2009). High-Spectral- and High-Temporal-Resolution Infrared Measurements from Geostationary Orbit. *Journal of Atmospheric and Oceanic Technology*, *26*(11), 2273–2292. https://doi.org/10.1175/2009JTECHA1248.1

Schneider, T., O'Gorman, P. A., & Levine, X. J. (2010). Water Vapor and the Dynamics of Climate Changes. *Reviews of Geophysics*, *48*(3). https://doi.org/10.1029/2009RG000302

Sherwood, S. C., Roca, R., Weckwerth, T. M., & Andronova, N. G. (2010). Tropospheric water vapor, convection, and climate. *Reviews of Geophysics*, *48*(2). https://doi.org/10.1029/2009RG000301

Smith, W. L., Feltz, W. F., Knuteson, R. O., Revercomb, H. E., Woolf, H. M., & Howell, H. B. (1999). The Retrieval of Planetary Boundary Layer Structure Using Ground-Based Infrared Spectral Radiance Measurements. *Journal of Atmospheric and Oceanic Technology*, *16*(3), 323–333. https://doi.org/10.1175/1520-0426(1999)016<0323:TROPBL>2.0.CO;2

Smith, W. L., Zhang, Q., Shao, M., & Weisz, E. (2020). Improved Severe Weather Forecasts Using LEO and GEO Satellite Soundings. *Journal of Atmospheric and Oceanic Technology*, *37*(7), 1203–1218. https://doi.org/10.1175/JTECH-D-19-0158.1

Solomon, S., Rosenlof, K. H., Portmann, R. W., Daniel, J. S., Davis, S. M., Sanford, T. J., & Plattner, G.-K. (2010). Contributions of Stratospheric Water Vapor to Decadal Changes in the Rate of Global Warming. *Science*, *327*(5970), 1219–1223. https://doi.org/10.1126/science.1182488

Stegmann, D. P. (2020). *CRTM: Transmittance Coefficient Generation Package*.

Stegmann, P. G., Johnson, B., Moradi, I., Karpowicz, B., & McCarty, W. (2022). A deep learning approach to fast radiative transfer. *Journal of Quantitative Spectroscopy and Radiative Transfer*, *280*, 108088. https://doi.org/10.1016/j.jqsrt.2022.108088

Stevens, B., Brogniez, H., Kiemle, C., Lacour, J.-L., Crevoisier, C., & Kiliani, J. (2017). Structure and Dynamical Influence of Water Vapor in the Lower Tropical Troposphere. *Surveys in Geophysics*, *38*(6), 1371–1397. https://doi.org/10.1007/s10712-017-9420-8

Strow, L. L., Benson, R. G., Hannon, S. E., & Motteler, H. E. (1996). Fast computation of monochromatic infrared atmospheric transmittances using compressed look-up tables. *Optical Spectroscopic Techniques and Instrumentation for Atmospheric and Space Research II*, *2830*, 106–115. https://doi.org/10.1117/12.256107

Strow, L. L., Hannon, S. E., De Souza-Machado, S., Motteler, H. E., & Tobin, D. (2003). An overview of the AIRS radiative transfer model. *IEEE Transactions on Geoscience and Remote Sensing*, *41*(2), 303–313. https://doi.org/10.1109/TGRS.2002.808244

Thies, B., & Bendix, J. (2011). Satellite based remote sensing of weather and climate: Recent achievements and future perspectives. *Meteorological Applications*, *18*(3), 262–295. https://doi.org/10.1002/met.288

Trenberth, K. E., Dai, A., Rasmussen, R. M., & Parsons, D. B. (2003). The Changing Character of Precipitation. *Bulletin of the American Meteorological Society*, *84*(9), 1205–1218. https://doi.org/10.1175/BAMS-84-9-1205

Trenberth, K. E., Fasullo, J., & Smith, L. (2005). Trends and variability in column-integrated atmospheric water vapor. *Climate Dynamics*, *24*(7), 741–758. https://doi.org/10.1007/s00382-005-0017-4

Trenberth, K. E., Fasullo, J. T., & Kiehl, J. (2009). Earth's Global Energy Budget. *Bulletin of the American Meteorological Society*, *90*(3), 311–324. https://doi.org/10.1175/2008BAMS2634.1

Turner, E., Rayer, P., & Saunders, R. (2019). AMSUTRAN: A microwave transmittance code for satellite remote sensing. *Journal of Quantitative Spectroscopy and Radiative Transfer*, *227*, 117–129. https://doi.org/10.1016/j.jqsrt.2019.02.013

Ukkonen, P., Pincus, R., Hogan, R. J., Pagh Nielsen, K., & Kaas, E. (2020). Accelerating Radiation Computations for Dynamical Models With Targeted Machine Learning and Code Optimization. *Journal of Advances in Modeling Earth Systems*, *12*(12), e2020MS002226. https://doi.org/10.1029/2020MS002226

Veerman, M., Pincus, R., Stoffer, R., van Leeuwen, C., Podareanu, D., & van Heerwaarden, C. (2021). *Predicting atmospheric optical properties for radiative transfer computations using neural networks*. https://doi.org/10.1098/rsta.2020.0095

Vial, J., Bony, S., Stevens, B., & Vogel, R. (2017). Mechanisms and Model Diversity of Trade-Wind Shallow Cumulus Cloud Feedbacks: A Review. *Surveys in Geophysics*, *38*(6), 1331–1353. https://doi.org/10.1007/s10712-017-9418-2

Wang, P., Li, Z., Li, J., & Schmit, T. J. (2021). Added-value of GEO-hyperspectral Infrared Radiances for Local Severe Storm Forecasts Using the Hybrid OSSE Method. *Advances in Atmospheric Sciences*, *38*(8), 1315–1333. https://doi.org/10.1007/s00376-021-0443-1

Weinreb, M., Fleming, H. E., McMillin, L. M., & Neuendorffer, A. C. (1981). *Transmittances for the TIROS operational vertical sounder*. https://repository.library.noaa.gov/view/noaa/13429

Wick, G. A., Neiman, P. J., Ralph, F. M., & Hamill, T. M. (2013). Evaluation of Forecasts of the Water Vapor Signature of Atmospheric Rivers in Operational Numerical Weather Prediction Models. *Weather and Forecasting*, *28*(6), 1337–1352. https://doi.org/10.1175/WAF-D-13-00025.1

Wulfmeyer, V., Hardesty, R. M., Turner, D. D., Behrendt, A., Cadeddu, M. P., Di Girolamo, P., Schlüssel, P., Van Baelen, J., & Zus, F. (2015). A review of the remote sensing of lower tropospheric thermodynamic profiles and its indispensable role for the understanding and the simulation of water and energy cycles. *Reviews of Geophysics*, *53*(3), 819–895. https://doi.org/10.1002/2014RG000476

Zhang, Y., Rossow, W. B., & Stackhouse Jr., P. W. (2006). Comparison of different global information sources used in surface radiative flux calculation: Radiative properties of the near-surface atmosphere. *Journal of Geophysical Research: Atmospheres*, *111*(D13). https://doi.org/10.1029/2005JD006873

Zhou, D. K., Larar, A. M., Liu, X., Smith, W. L., Strow, L. L., Yang, P., Schlüssel, P., & Calbet, X. (2011). Global Land Surface Emissivity Retrieved From Satellite Ultraspectral IR Measurements. *IEEE Transactions on Geoscience and Remote Sensing*, *49*(4), 1277–1290. https://doi.org/10.1109/TGRS.2010.2051036

LIST OF ABBREVIATIONS

ABI	Advanced Baseline Imager
AI	Artificial Intelligence
AIRS	Atmospheric Infrared Sounder
BT	Brightness Temperature
CAMS	Copernicus Atmosphere Monitoring Service
CRTM	Community Radiative Transfer Model
ECMWF	European Centre for Medium-Range Weather Forecasts
ENSO	El Niño Southern Oscillation
ERA5	Fifth generation of ECMWF reanalysis
EUMETSAT	European Organisation for the Exploitation of Meteorological Satellites
GCM	General Circulation Model
GEO	Geostationary Earth Orbit
GeoXO	Geostationary Extended Observations
GOES	Geostationary Operational Environmental Satellite
HAPI	HITRAN Application Programming Interface
HITRAN	HIgh-resolution TRANsmission molecular absorption database
IFS	Integrated Forecast System
IR	Infrared
IWV	Integrated Water Vapor
LBLATM	MonoRTM program generating vertical pressure grid
LBLRTM	Line-by-Line Radiative Transfer Model
LEO	Low-Earth Orbit
LNFL	HITRAN line file creation program in MonoRTM
LW	Longwave
ML	Machine Learning
MODIS	Moderate Resolution Imaging Spectroradiometer
MODM	Monochromatic Optical Depth Model of MonoRTM

MonoRTM	Monochromatic Radiative Transfer Model
MT_CKD	Continuum absorption model
MW	Microwave
NN	Neural Network
NOAA	National Oceanic and Atmospheric Administration
NWP	Numerical Weather Prediction
ODAS	Optical Depth on Absorber Space
ODPS	Optical Depth on Pressure Space
OLR	Outgoing Longwave Radiation
OPTRAN	Optical Path Transmittance
PLOD	Pressure Level Optical Depth
RT	Radiative Transfer
RTMmono	The radiative transfer code in MonoRTM
RTTOV	Radiative Transfer for Television and infrared Observation satellite operational Vertical sounder
SNR	Signal-to-Noise Ratio
SRF	Spectral Response Function
SST	Sea Surface Temperature
SW	Shortwave